Bachelor's Thesis

Eine Studie über Methoden zur Rekonstruktion der invarianten di-tau Masse im ATLAS am LHC

A study of the di-tau invariant mass reconstruction techniques in ATLAS at LHC

prepared by

Art Gabriel

from Henstedt-Ulzburg

at the II. Physikalischen Institut

Thesis number:	II.Physik-UniGö-BSc-2014/08
Thesis period:	14th April 2014 until 18th July 2014
First referee:	Prof. Dr. Arnulf Quadt
Second referee:	Prof. Dr. Ariane Frey

Abstract

The goal is to measure the direct decay of the Higgs boson to a di-tau system, to achieve this the knowledge and understanding of the behaviour of the reconstruction methods is of great significance. In this thesis the collinear approximation and the MMC algorithm are compared on the variation of different parameters.

Monte Carlo data on VBF, gg H$\to \tau^+\tau^-$ and on Z$\to \tau^+\tau^-$ physics processes for $\sqrt{S} = 8\,\text{TeV}$ are studied. The MMC algorithm has an overall better performance in relation to the resolution and efficiency in comparison to the collinear approximation.

Contents

Contents

Nomenclature

Latin Letters

Variable	Meaning	Unit ($\hbar = c = 1$)
$\mathcal{L}$	Lagrangian density	-
A_μ	Gauge field	-
$F_{\mu\nu}$	Energy-momentum tensor	-
m	Mass	[GeV]
p	Absolute value of the momentum	[GeV]
p_T	Transverse mass	[GeV]
E	Energy	[GeV]
E_T	Transverse energy	[GeV]
$\not{E}_T$	Missing transverse energy	[GeV]
y	Rapidity	-
v	Velocity	-
Q^2	Squared four momentum	[GeV^2]
$\sqrt{s}$	Center of mass energy	[GeV]
BR	Branching ratio	-
f_{fit}	Gaussian fitting function	-
a	Parameter of Gaussian function	-
C	Cut	-

Greek Letters

Variable	Meaning	Unit ($\hbar = c = 1$)
γ^μ	Dirac matrices	-
ψ	Wave function	-

Variable	Meaning	Unit ($\hbar = c = 1$)
η	Pseudo rapidity	-
ν	Transferred energy	[GeV]
σ	Cross section	[pb]
ϕ	Azimuthal angle	-
θ	Polar angle	-
α	Angle between tau leptons	-
μ	Mean of the Gaussian function	[GeV]
σ'	Standard deviation of the Guassian function	[GeV]

Indices

Index	Meaning
mis	Missing
vis	Visible
res	Resonance
T	Transverse
Z	Z boson
H	Higgs boson
τ	Tau lepton
$\tau\tau$	Di-tau
jet	Jet
1	Leading
2	Subleading
reco	Reconstruction
int	Missing transverse energy intersects tau leptons
not int	Missing transverse energy does not intersect tau leptons
default	Default (Cut always applied)
all	All (All cuts applied)

Abbreviations

Abbreviation	Meaning
SM	standard model
ECAL	Electromagnetic calorimeter
HCAL	Hadronic calorimeter
CERN	Conseil Européen pour la Recherche Nucléaire
LHC	Large Hadron Collider
ATLAS	A Toroidal LHC Apparatus
SLAC	Stanford Linear Accelerator Center
MMC	Missing Mass Calculator
LO	Leading order
NLO	Next to leading order
VBF	Vector boson fusion
gg	Gluon-gluon fusion
ID	Identification
BDT	Boosted decision trees

List of Figures

List of Tables

1 Introduction

Particle physics is the most fundamental field in physics. The elementary particles and forces, gravitation excluded, are explained by the standard model of particle physics. This theoretical structure predicted a majority of the discoveries in the field of high energy physics and is therefore the most successful theory in its field. The theoretical model initiated an avalanche of Nobel prizes, the Higgs boson being one of the most recent Nobel prize winning particle physics topics.

The Higgs boson was discovered in bosonic decay channels. To acquire proof of the Higgs boson decaying to tau leptons the resonance in the mass distribution of the leptons must be found. This thesis tries to work towards this goal by studying the reconstruction techniques of the di-tau invariant mass. The reconstruction is quite challenging since at least two neutrinos are involved in the di-tau decay. With sophisticated methods it is, however, possible to determine the di-tau invariant mass. The Missing Mass Calculator (MMC) is an algorithm reconstructing the di-tau invariant mass and promises good results in the distinction of the signal from the background processes.

The behaviour of this reconstruction algorithm is applied to di-tau hadronic decays and studied by the variation of several parameters.

The starting point is a brief theoretical introduction of the standard model in Chapter 2 followed by an explanation of the experimental setup in Chapter 3. The behaviour of colliding hadrons, the decay channels of the tau lepton and the Z boson are discussed. Furthermore, two Higgs boson production channels are examined. A sketch of the framework of the particle detector ATLAS is supplied and afterwards the di-tau system, its decay and the reconstruction of the di-tau invariant mass is explained.

In Chapter 4 the origin of the data analysed in this thesis is mentioned. Afterwards, the event selection is inspected just before heading into the analysis in Chapter 6. The thesis is concluded in Chapter 7.

2 Standard Model of Particle Physics

In this section, look at the theoretical fundamentals needed later is taken. There are no full explanations given here. For a more thorough explanation on the topic see for example [1].

The Standard Model (SM) of particle physics is a theory which successfully describes the electromagnetic, weak and strong interactions between particles but does not account for the gravitational force. In particle physics, the gravitational force is negligible because the only interest usually lies in systems with small rest mass and high energies.

2.1 Elementary Particles

The SM contains 61 elementary, point-like particles. These particles are listed and sorted in Figure 2.1. Of these 61 particles there are 12, so called fermions, of spin-$\frac{1}{2}$ which can be separated by their type of interaction: the quarks and leptons. Each quark carries one of three colour charges and interacts via the strong force. The quarks are sorted by their mass into three generations and paired by the electrical charge. The leptons do not carry such a colour charge. There are also three generations of leptons. Each electrically charged lepton is paired with the corresponding uncharged neutrino. Leptons interact weakly and electromagnetically, if carrying an electric charge. For each fermion there exists an antiparticle of opposite charge but with equal mass.

In addition to the fermions there are also gauge bosons included in the standard model. These bosons are the mediators of the forces. The gauge bosons are predicted by gauge theories. The vector bosons of the weak force are the $W^{\pm}$ and the Z boson. The gauge boson for the electromagnetic force is the photon and for the strong force the gluons mediate the interactions. The Higgs boson is responsible for the mass of all particles.

Figure 2.1: The SM of elementary particles with three generations of fermions and the gauge bosons. The quarks are coloured blue, the leptons green and the bosons red excluding the black Higgs boson.

2.2 Gauge Theories

A gauge theory is a field theory in which the dynamics of a system are described by a Lagrangian function which is required to be invariant under a continuous group of local transformations, the gauge transformations.

For three different symmetry groups the gauge bosons for the different forces are obtained. These bosons are interpreted to be the mediator of the corresponding force. If invariance is demanded of the Lagrangian, these particles must be massless. The mass term of those particles would spoil the invariance and this is where the Higgs mechanism is needed. The observed gauge bosons are the photon for the electromagnetic, the $W^{\pm}$ and Z^0 for the weak and eight gluons for the strong force. The mediators of the weak force are observed to have a mass.

As an example look at the Dirac Lagrangian can be taken, which has the following form:

$$\mathcal{L} = i\hbar c\bar{\psi}\gamma^{\mu}\partial_{\mu}\psi - mc^2\bar{\psi}\psi \tag{2.1}$$

A global gauge transformation

$$\psi(x) \rightarrow e^{i\alpha}\psi(x) \tag{2.2}$$

$$\bar{\psi}(x) \rightarrow e^{-i\alpha}\bar{\psi}(x) \tag{2.3}$$

is promoted to a local one by introducing a time and space dependence of the parameter $\alpha \to \alpha(x) = \alpha(t, \vec{x})$. As one can see there would now be extra terms from the derivative. These additional terms break the invariance. In order to have a gauge invariant Lagrangian a gauge field A_μ which transforms as follows must be added:

$$A_\mu \to A_\mu + \partial_\mu \frac{\hbar c}{q} \partial^\mu \alpha \tag{2.4}$$

The new Lagrangian is then invariant under local gauge transformation

$$\mathcal{L} = \left(i\hbar c \bar{\psi} \gamma^\mu \partial_\mu \psi - mc^2 \bar{\psi}\psi \right) - (q\bar{\psi}\gamma^\mu\psi)A_\mu \tag{2.5}$$

In addition the Lagrangian is required to contain a free term for the gauge field. For a vector field one can take a look at the Proca Lagrangian

$$\mathcal{L} = \frac{-1}{16\pi} F^{\mu\nu} F_{\mu\nu} + \frac{1}{8\pi} \left(\frac{m_A c}{\hbar} \right)^2 A^\nu A_\nu \tag{2.6}$$

with the energy momentum tensor $F^{\mu\nu} = \partial^\mu A^\nu - \partial^\nu A^\mu$. The energy momentum tensor is invariant, but $A_\mu A^\mu$ is not. The term spoils the invariance and must vanish. Therefore, the mass must vanish. The intermediate vector bosons do have a mass and this is where the Higgs mechanism is needed.

2.2.1 The Higgs Mechanism

The Higgs mechanism solves this problem. It was firstly introduced by Higgs [2]. Two other groups also introduced the theoretical mechanism. One group from the Université Libre de Bruxelles formed by Englert and Brout [3] and the other group from the Imperial College formed by Kibble, Hagen and Guralnik [4]. Higgs was the first to predict the existence of the Higgs particle which is why this mechanism is often called only by his name.

To find a term with the interpretation of the mass in the Lagrangian one usually expands the Lagrangian about its ground state. The Lagrangian can have multiple ground states. Breaking this symmetry by choosing only one and afterwards choosing the gauge for the Lagrangian yields a new particle, the Higgs boson, responsible for the mass of the $W^\pm$ and Z^0 bosons as well as for all other particles. In Figure 2.2 the ground states are schematically represented. Breaking the symmetry does not alter the physics, it is merely a notational tool to identify the mass term. The Higgs mechanism conserves the gauge invariance and also accounts for the masses of the $W^\pm$ and Z^0 bosons.
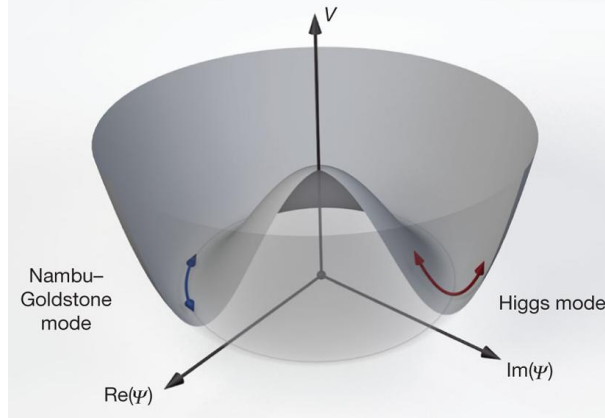
Figure 2.2: Visual representation of the Lagrangian and its ground states. The Higgs and the Goldstone modes are marked with red and blue arrows accordingly. Illustration taken from [5].

To look at the details of this mechanism, the calculation starts out with following Lagrangian containing the two real fields ϕ_1 and ϕ_2:

$$\mathcal{L} = \frac{1}{2}(\partial_\mu \phi_1)(\partial^\mu \phi_1) + \frac{1}{2}(\partial_\mu \phi_2)(\partial^\mu \phi_2) + \frac{1}{2}\mu^2(\phi_1^2 \phi_2^2) - \frac{1}{4}\lambda^2 \mu^2 (\phi_1^2 \phi_2^2)^2 \tag{2.7}$$

This Lagrangian can be rewritten neatly by combining the two fields $\phi = \phi_1 + i\phi_2$ and $\phi^*\phi = \phi_1^2 + \phi_2^2$. It therefore follows:

$$\mathcal{L} = \frac{1}{2}(\partial_\mu \phi)^*(\partial^\mu \phi) + \frac{1}{2}\mu^2(\phi^*\phi)^2 - \frac{1}{4}\lambda^2(\phi^*\phi)^2 \tag{2.8}$$

The potential depicted in 2.2 requires $\mu^2 < 0$ and $\lambda > 0$. To get local gauge invariance the gauge field A_μ is introduced, as before.
I use the covariant derivative $\mathcal{D}_\mu = \partial_\mu + i\frac{q}{\hbar c}A_\mu$ and get:

$$\mathcal{L} = \frac{1}{2}(\mathcal{D}_\mu \phi)^*(\mathcal{D}^\mu \phi) + \frac{1}{2}\mu^2(\phi^*\phi)^2 - \frac{1}{4}\lambda^2(\phi^*\phi)^2 - \frac{1}{16\pi}F^{\mu\nu}F_{\mu\nu}$$

The fields are defined as $\eta = \phi_1 - \frac{\mu}{\lambda}$ and $\xi = \phi_2$ according to the ground states of the Lagrangian. This leads to the following Lagrangian

$$\mathcal{L} = \left[\frac{1}{2}(\partial_\mu \eta)^*(\partial^\mu \eta) - \mu^2 \eta^2\right] + \left[\frac{1}{2}(\partial_\mu \xi)^*(\partial^\mu \xi)\right]$$
$$+ \left[\frac{1}{16\pi}F^{\mu\nu}F_{\mu\nu} + \frac{1}{2}\left(\frac{q\mu}{\hbar c\lambda}\right)^2 A_\mu A^\mu\right] - 2i\left(\frac{q\mu}{\hbar c\lambda}\right)(\partial_\mu \xi)A^\mu$$
$$+ \{... \text{ couplings of } \xi, \eta \text{ and } A^\mu ...\} + \left(\frac{\mu^2}{2\lambda}\right)^2$$

We thus acquired a mass term. The first line describes the scalar particle and a massless Goldstone boson. The second line describes the gauge field, which has a mass of $m_A = 2\sqrt{\pi}\frac{q\mu}{\lambda c^2}$. To get rid of the Goldstone boson, which is not and cannot be observed, one simply chooses a different gauge that eliminates the boson.

As a result of the whole procedure one gained a mass carrying gauge field and a scalar particle also carrying a mass, the Higgs boson. It is important to realize that the physics was not altered, but merely the notation. The Higgs boson was not created by the notation but rather revealed by it. The Higgs mass is then $m_\eta = \sqrt{-2\mu^2}$.

2.2.2 Quantum Field Theory

The modern quantum field theory hands us most of the tools to calculate even complicated interactions in particle physics. It is formed by the gauge theories and the requirement for a renormalizable theory. It combines the classical field theory with quantum mechanics, unifying particles and forces by describing both with fields.

Quantum field theory is often depicted in the form of so called Feynman diagrams. These diagrams, named after Richard Feynman, put the complicated formulas into a form in which it is much easier to keep track of the general structure of an interaction. Each symbol in the Feynman diagrams corresponds to a factor in the matrix element used to calculate the cross section of a certain interaction. Further explanations on this topic can be found in [6].

From now on natural units are used, where $\hbar = c = 1$.

3 Experimental Setup

3.1 Inside the Detector

Detectors play a great role in high energy physics. The nature of their construction determines not only the accuracy of the results but also the tools for analyzing the results. In this section, some basic kinematic quantities will be discuessed first and then the structure of the ATLAS detector is talked about, since the data samples used for this thesis are taken from the ATLAS experiment. These two topics are followed by an explanation of how the particles are identified by the detector.

3.1.1 Kinematics

There are many different kinematic variables that can be measured, but the ones that will yield meaningful results are determined by the kinematics of the reaction itself. In the proton-proton reaction, the longitudinal momentum (the momentum in the direction of the beam axis) is unknown for the partons, and thus the energy of the final products is also unknown. The parton distribution function of the proton is the explanation for this behaviour. One does not know which particles react and each parton inside the proton carries a different fraction of momentum as explained in Section 3.2. In the detector it is therefore sensible to mainly measure the transverse momentum defined as $p_T = \sqrt{p_x^2 + p_y^2} = \frac{p}{\cosh \eta}$. Here η is the pseudo-rapidity defined as $\eta = -\ln\left(\tan\left(\frac{\theta}{2}\right)\right)$ with θ being the angle between the momentum and the beam axis. The transverse momentum must be conserved. The transverse energy is defined by the transverse momentum as $E_T = E \cdot \sin \theta$.

Since the particle colliders operate at different energies, the introduction of the rapidity is needed. Results from the different detectors should be comparable. The rapidity y is defined by the speed of light c and velocity ν as follows:

$$y = \frac{1}{2} \log\left(\frac{E + p_z c}{E - p_z c}\right) = \tanh^{-1}\left(\frac{p_z}{E}\right)$$

where E is the energy and p_z the momentum in longitudinal or z direction. The z direction is the direction of movement of the particle. Rapidity intervals are Lorentz invariant, making it a comparable quantity.

3.1.2 The ATLAS Detector

The data which is to be analysed in the thesis is taken from ATLAS [7], a particle detector at the Large Hadron Collider (LHC) [8] at CERN. The LHC is the particle accelerator with the highest centre-of-mass energy in the world. The ring making up this accelerator has a length of 27 km and was powered up in 2008 for the first time. The LHC accelerates protons in opposite direction in two separate beam pipes. A look at the layering of detector elements of ATLAS pictured in Figure 3.1 will be taken next. The detector contains layers of detection elements with different purposes. The innermost detection element is the pixel detector followed by a semiconductor tracker. Both detectors track the particles' trajectory.

In the **pixel detector**, a charged particle ionizes the material. These free charges instantly induce a mirror charge in the pixels. The length of the electric pulse in each pixel determines the initial ionization position where the particle hit the detector material. Layering these pixel detectors yields a three dimensional reconstruction of the trajectory of a charged particle.

The **semiconductor tracker** works similar to a diode. The junction of an n-doped and p-doped material creates, upon diffusion of charge carriers, a depletion zone. The charge carriers combine in the other material and are stationary thus creating a stable electric field counteracting the diffusion. If a positive potential is connected to the n-doped material and vice versa, then the depletion zone grows. The depletion zone can be extended throughout the whole material. Any cascade created by an incident particle can now easily be detected by measuring the current.

The next detection element is the **transition radiation tracker**. A charged particle radiates off photons when passing a junction of two different materials. A different index of refraction in each material yields a change in electric fields, or in other words, radiation of photons. The faster a particle is, the less it radiates. The greater the rest mass of a particle is, the less it radiates upon transition.

The inner detector has a coverage over the pseudorapidity interval $|\eta| < 2.5$. The **solenoid magnet** is placed after the trackers with a axial magnetic field of 2 T and has a length of 5.3 m with a bore of 2.4 m. The magnetic field bends the trajectory of electrically charged particles. With the magnetic field not only the positioning but also the momentum of particles can be measured by the trackers.

The next layer consists of the **calorimeters**. The calorimeters are separated into an electromagnetic (ECAL) and a hadronic (HCAL) one. The incident particles interact with an absorber material, causing particle and radiation showers. For hadronic interactions jets may be formed hitting the calorimeter. The jets hit the detector material forming new jets inside the detector. These jets are also called hadronic showers and are explained in Section 3.2.1. Jets and therefore the hadrons are mostly detected in the hadronic calorimeter. Another type of showers can be caused by electrons or photons. The electrons or photons ionize atoms, kicking out further electrons. The electrons can radiate Bremsstrahlung in the form of photons which can again ionize the material. This sort of shower is called an electromagnetic shower. These two kinds of showers can then be detected in the active material. This layering of absorber and active materials is called sampling. The sampling construction allows for a more compact calorimeter than a homogeneous architecture would. However some particles in the showers may already be fully stopped within the absorber material, resulting in a smaller measured energy. The hadronic calorimeter has a coverage over the pseudorapidity interval of $|\eta| < 4.9$.

The outermost element is the **muon chamber**. The muon chambers are positioned in the outermost layer of the detector because the muons barely interact with the calorimeter materials at all and thus are the only particles reaching this layer. The muon chambers also contain one of the three trigger systems of the ATLAS detector.
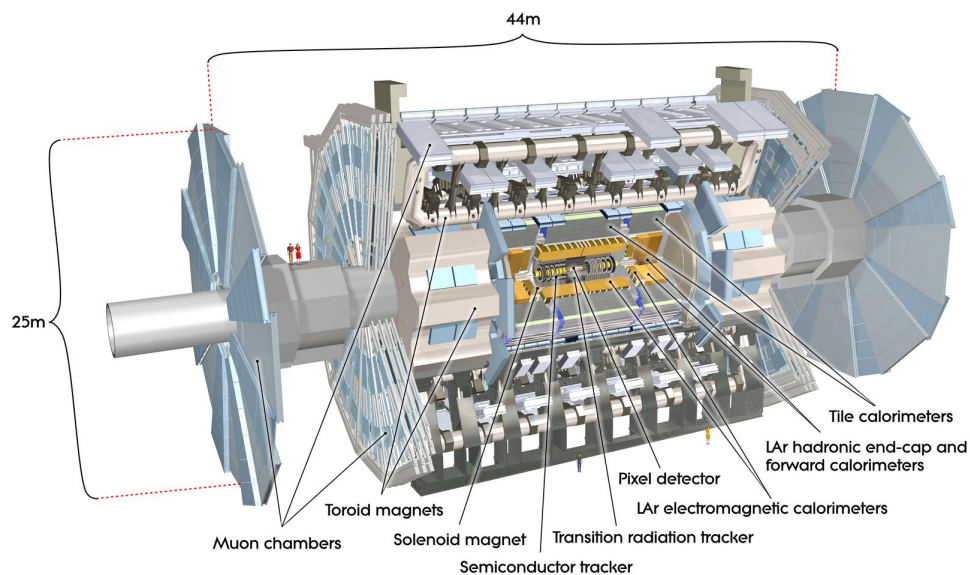

Figure 3.1: The ATLAS detector in a schematic visualization with labeled elements taken from [9].

3.1.3 Particle Identification

Hadrons will deposit most of their energy in the HCAL. They also interact with the material of the ECAL since they might be charged, but will only deposit very little energy in the ECAL. Charged hadrons are also detected by the trackers. Electrons are observed by the trackers but deposit all of their energy within the ECAL. Almost no energy should be left to be detected by the HCAL. The tau lepton as well is not as easy to detect and the muon is barely detected by the calorimeters at all. Since muons have a greater mass than electrons and thereby a higher critical energy E_C they radiate almost no bremsstrahlung at operating energies of the ATLAS. In Figure 3.2 the stopping power for muons in copper is plotted against the muon momentum. The lifetime of the tau is very short as stated in Section 3.5. The tau decays before being detected in the calorimeters. If a jet is produced by the tau it is narrow compared to the ones created in QCD processes. The tau can also decay into leptons. The neutrinos cannot be detected at all. They do not carry any charge and are very light, so basically do not interact with any matter at all. To identify the neutrinos one uses momentum-energy conservation. This conservation only applies to the transverse momentum and energy. The missing momentum must be carried away by the neutrinos, assuming a perfect detector. The momentum of the neutrino is

$$\vec{E}_T^{\text{mis}} = -\sum_i p_T^i$$

where the sum runs over the transverse momenta of all the visible final state particles.

3.2 The Proton

The proton is a composite particle, a baryon. The proton consists of three valence quarks: two up-quarks and one down-quark. The rest masses of those valence quarks only contribute about 1 % to the proton's mass. The remaining fraction arises from the so called sea quarks and gluons. The valence quarks interact with one another constantly, radiating off gluons, creating new quarks with much lower energies. The momentum-fraction of the total proton-momentum carried by each particle is determined by the parton distribution functions in Figure 3.3. The probability of finding a certain particle with the corresponding momentum is assigned to the y-axis. The Bjorken-x is the momentum-fraction $x = Q^2/2M\nu$ and is assigned to the x-axis. In this, the variable Q^2 is the square of the four momentum, $\nu = E - E'$ the transferred energy and the mass M.

On the left side in Figure 3.3, the squared four momentum exchange Q^2 is four orders of magnitude smaller than in the right diagram. The gluon distribution is shown scaled
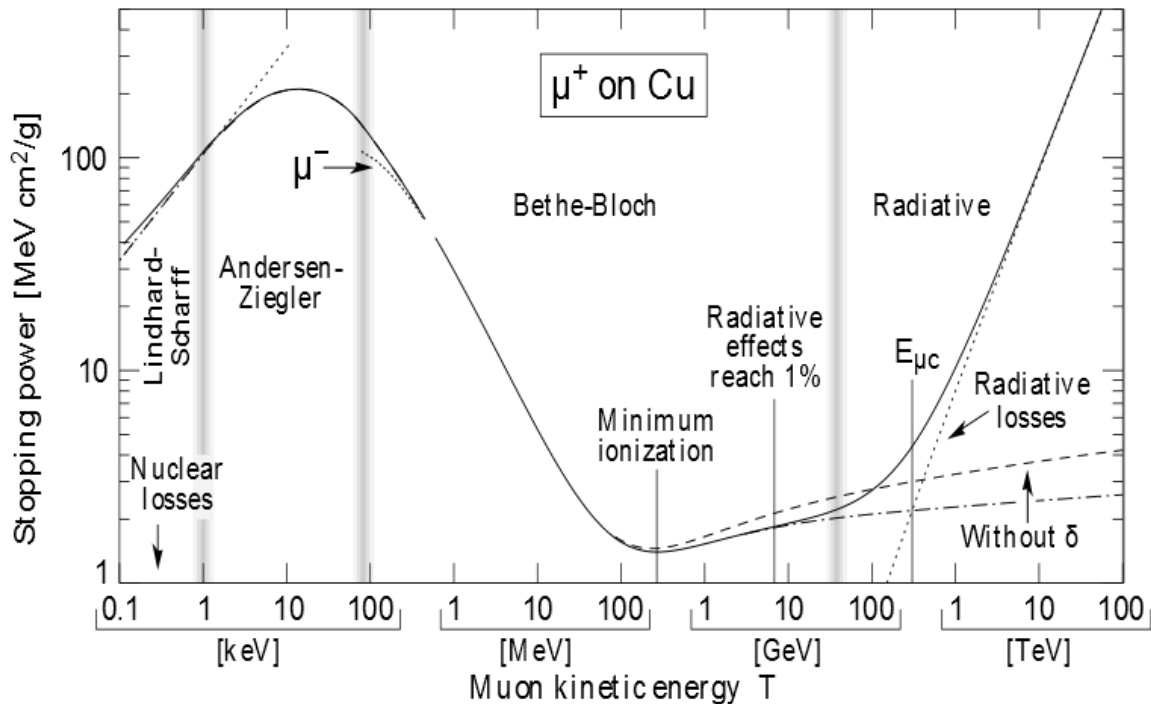
Figure 3.2: The muon stopping power of copper depending on the muon momentum. Figure taken from [10].

down with a factor of 10. On the right side one can see that the gluons dominate all the other distributions.

3.2.1 Proton-Proton Reaction

The interaction of two particles can be described using the Feynman rules mentioned in Section 2.2.2. Applying those rules to a reaction allows us to calculate the probabilities of all outcomes. The Feynman rules are only estimations and not exact, although one can calculate the probabilities to a desired degree of accuracy by considering higher order terms.

When two accelerated protons interact with one another, new particles are created corresponding to the energies of the two protons. The interaction must not be between two valence quarks of the protons but can also occur between two sea gluons. New particles created cannot have a greater total energy than the initial particles.

At low energies the proton-antiproton reaction yields more available energy than the proton-proton reaction for the created particles. Two valence quarks can annihilate whereas for the proton-proton reaction a valence quark can only annihilate with a sea quark. In the graph in Figure 3.3 the Bjorken-x is inversely proportional to the energy of

13
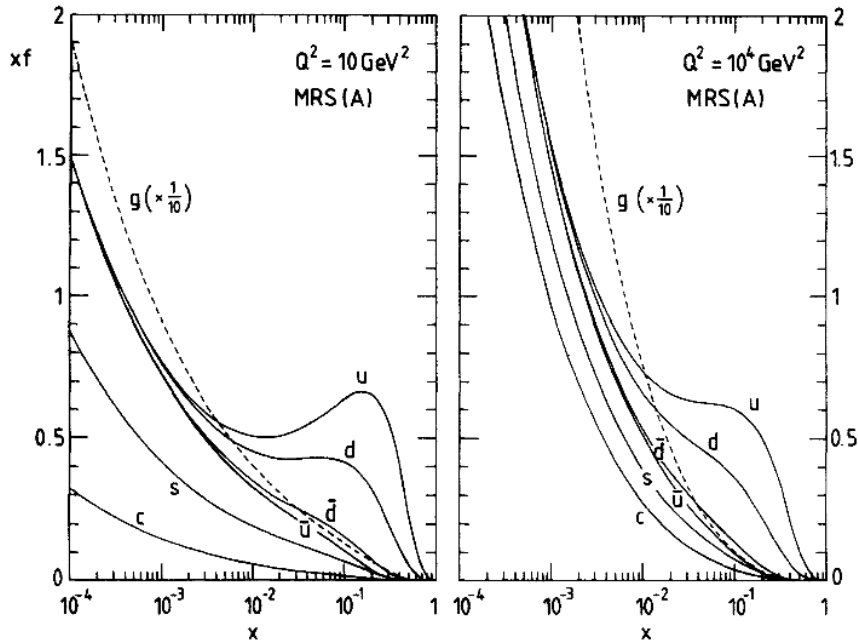
Figure 3.3: The parton distribution functions for the proton. The x-axis shows the Bjorken-x and the y-axis shows the probability to find a certain particle with the corresponding Bjorken-x. The picture is taken from [11].

the proton. The higher the energy of the proton, the greater is the fraction of momentum carried by sea particles. At high energies the particles reacting are mainly gluons, thereby rendering the difference between proton-proton and proton-antiproton reactions negligible. In contrast to elementary particles the cross-section for a proton-proton reaction rises after hitting a minimum. The vertex factor for this reaction depends on the inverse of the energy and one could expect a cross-section that decreases with rising energy. The parton distribution function explains the rise in the cross-section. With higher energies more sea particles are available for interaction, yielding a greater cross-section. This counteracts the vertex factor, overwhelming it after the minimum.

The interaction of the partons from the two protons may cause the bound quarks to scatter. The strong interaction becomes stronger for larger distances between the quarks originating from the hadron. This increase in the potential causes the creation of new particles. The newly created particles replace the original bond partner from the hadronic state. All free objects found in nature are colourless and thus the partons that were ripped apart must form new bonds to create colourless objects. This process is called hadronisation or fragmentation. This procedure is repeated and thus a cascade of hadrons is created. These showers are also called jets. Not only quarks but also gluons can form

jets.

The rest of the partons from the two protons may also interact, even though at smaller energies. These interactions and left over partons together with other interactions from the remaining protons in the bunch make up the so called underlying event.

3.3 The Z Boson

The Z boson is the neutral gauge boson of the weak force with a mass of $m_Z = (91.1876 \pm 0.0021)\,\text{GeV}$ [12]. The mediators of the weak force are the intermediate vector bosons Z and $W^{\pm}$. They were predicted in the 1960's by Glashow, Salam and Weinberg who unified the electromagnetic and weak force to the electroweak force [13–15]. In 1979 all of them received the Nobel prize for this accomplishment. The neutral weak interaction was observed shortly after its prediction in the Gargamelle bubble chamber experiment at CERN in the form of neutral currents [16, 17]. The intermediate vector bosons were observed directly in 1983 at the SPPS in the detectors UA1 [18] and UA2 [19]). Rubbia was in charge of the UA1 and Darriulat lead the UA2. The stochastic cooling developed by van der Meer was used in the SPS. In 1984 Rubbia and van der Meer received the Nobel prize for this discovery.

At the LEP precision measurements determined the Z boson properties with very high accuracy. The Z boson may decay into tau pairs. Since the mass is very well known one can test mass reconstruction techniques on this decay with the possibility of cross checking the reconstructed mass with the known Z mass.

3.4 The Higgs Boson

The neutral Higgs particle is the heaviest boson with a mass of $m_H = (125.9 \pm 0.6)\,\text{GeV}$. The discovery was announced on the 4th of July in 2012 at CERN. Independently and simultaneously the ATLAS collaboration [20] and the CMS collaboration [21] confirmed the discovery of a new particle. Much later on the 13th of March in 2013, it was announced to be a Higgs boson. The observed Higgs width is consistent with the SM prediction for its lifetime. The Higgs boson has not yet been observed to couple to fermions but there is evidence of it [22, 23]. Couplings to the intermediate vector bosons have been seen. The Higgs boson can decay into photons with the step of a W boson loop in between. The Higgs boson couples to mass and thus a coupling to the bottom quark or the tau lepton are expected to be the likeliest to observe. The top quark is too heavy to be a decay product of the Higgs boson.

3.4.1 Production

The Higgs boson can be produced in many different ways in a hadron collider. The dominating production mechanisms are the gluon-gluon fusion (gg) and the vector boson fusion (VBF).

The quarks within the proton may radiate off vector bosons. Those bosons can fuse and thereby create the Higgs boson. A Feynman diagram of the VBF followed by the Higgs boson decaying into a $\tau^+\tau^-$ pair is shown in Figure 3.4. The cross section for this Higgs boson production is $\sigma = 1.559^{+3\%}_{-2.8\%}$ pb for $\sqrt{s} = 8$ TeV and a Higgs boson mass of $m_H = 125$ GeV [24].
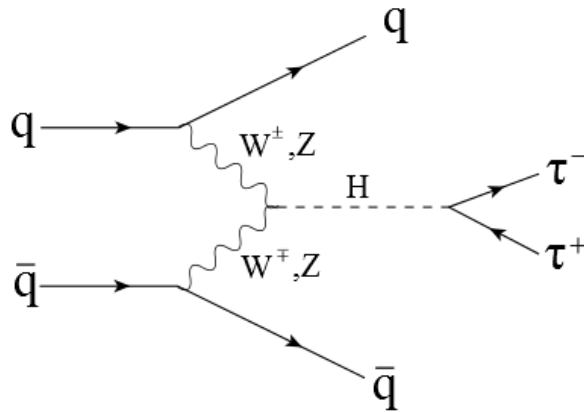
Figure 3.4: Feynman diagram for VBF leading to a H$\rightarrow \tau^+\tau^-$ process.

As mentioned in Section 3.2, the interaction between two protons can often be mediated by a gluon-gluon interaction. The two gluons can fuse and create the Higgs boson. In Figure 3.5, the Feynman diagram for a gg creating a Higgs boson, leading into a $\tau^+\tau^-$ pair decay is shown. The cross section for gluon fusion producing a Higgs boson is $\sigma = 19.52^{+14.7\%}_{-14.7\%}$ pb for $\sqrt{s} = 8$ TeV and a Higgs boson mass of $m_H = 125$ GeV [24]. This cross section is significantly higher than the one from the VBF channel.

3.4.2 Decay

The Higgs boson can in theory decay into any particle but the top quark. The top quark is heavier than the Higgs boson. In Figure 3.6, the different decay channels with their branching ratios are drawn in a pie chart. The only one relevant to this thesis is the decay into a τ pair. As mentioned before, only the coupling to the vector bosons and the indirect decay to photons have been seen. For the coupling of the Higgs boson to the tau lepton the evidence was mentioned above.
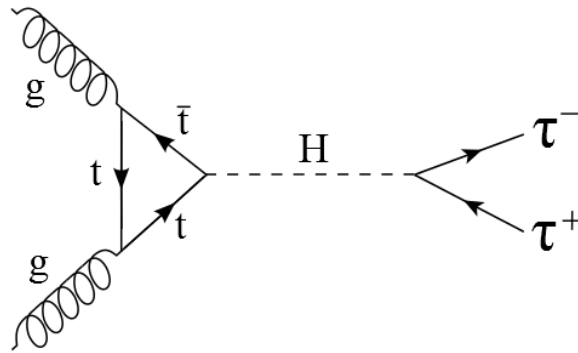
Figure 3.5: Feynman diagram for gg leading to a H$\to \tau^+\tau^-$ process.
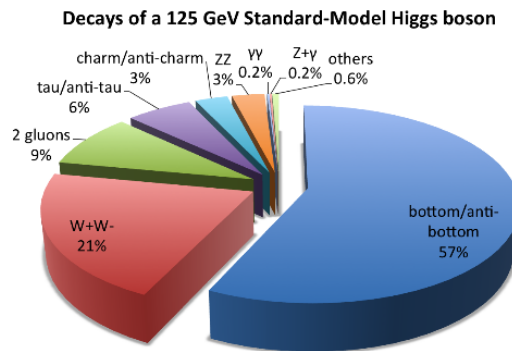
Figure 3.6: Branching ratio of the Higgs boson for $m_H = 125\,\text{GeV}$.

3.5 The Tau Lepton

The tau is the heaviest lepton with a mass of $m_\tau = (1.777 \pm 0.16)\,\text{MeV}/c^2$ [12] and belongs to the third generation of the lepton family. The tau was discovered in 1975 by Perl and his group at SLAC [25]. Perl received the Nobel prize in 1995 for this discovery. Unlike the electron it is not a stable particle. The mean lifetime of a tau is merely $(290.6 \pm 1.0) \times 10^{-15}$ s [12]. Unlike all other leptons, it can decay into hadrons because of its large mass. The hadronic decay is mediated by the weak force. The hadronic decay can be classified by the number of charged particles the tau decays into. For one charged particle the decay is called a 1-prong hadronic decay and for three charged particles it is called a 3-prong hadronic decay. A leptonic decay is also possible via the weak interactions. All branching ratios, the masses and the lifetimes in the following are taken from [12].

3.5.1 The Leptonic Tau Decay

The tau lepton can decay leptonically into either a tau neutrino, electron and electron antineutrino or a tau neutrino, muon and muon antineutrino. The leading diagrams are

shown in Figure 3.7. The branching ratios are $BR = (17.83 \pm 0.04)$ % for the electron decay and $Br = (17.41 \pm 0.04)$ % for the muon decay.
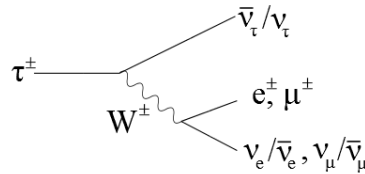
Figure 3.7: Feynman diagram for the leptonic tau decay. Arrows on the particle lines are left out for generality of both particle and anti-particle decays.

3.5.2 The 1-Prong Hadronic Tau Decay

The most likely hadronic decay of the tau lepton is the decay into a tau neutrino, a charged pion and a neutral pion with a probability of $BR = (25.52 \pm 0.09)$ %. Other possibilities are with $BR = (10.63 \pm 0.06)$ % the decay into a tau neutrino and a charged pion and with $BR = (9.30 \pm 0.11)$ % the decay into a tau neutrino, two neutral pions and a charged pion. The Feynman diagram for the single charged pion decay is shown in Figure 3.8. Also a decay into three neutral pions and one charged pion occurs with a probability of (1.05 ± 0.07) %
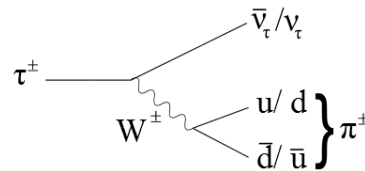
Figure 3.8: Feynman diagram representing the 1-prong tau decay, namely the decay into one charged pion and no neutral pions. Arrows on the particle lines are left out for generality of both particle and anti-particle decays.

3.5.3 The 3-Prong Hadronic Tau Decay

The 3-prong decays are more rare than the 1-prong or purely leptonic decays. The most common is the decay into a tau neutrino and three charged pions with a total charge of the decaying tau with about $BR = (8.99 \pm 0.06)$ %. Two pions must have the same charge. Another decay is into a tau neutrino, three charged pions, of which again two have the same charge, and a neutral pion with $BR = (2.70 \pm 0.008)$ %.
The overall branching ratio to hadrons is about 65 % and to leptons 35 %.

3.6 The Di-Tau System

The Higgs boson can decay in many different channels. One of them is the di-tau channel
(H$\to \tau\tau$). Reconstructing the mass of the di-tau system should then yield the mass of the
Higgs boson. This would be a sign of the Higgs boson coupling to leptons. The largest
branching ratio of the leptonic decay of the Higgs boson is expected to be the di-tau
decay, since tau leptons are the heaviest leptons and the Higgs couples proportionally to
the fermion mass.

3.6.1 Di-Tau Decay

The di-tau system can decay in three different modes, as explained in Section 3.5. Either it
decays fully leptonically, semileptonically or fully hadronically. For each decay a different
number of neutrinos is produced;

- 4 neutrinos in the lepton-lepton channel.

- 3 neutrinos in the lepton-hadron channel.

- 2 neutrinos in the hadron-hadron channel.

Since the energy carried by the invisibly decaying particles is non-zero, the visible di-tau
mass is always smaller than the expected invariant mass. The missing transverse momen-
tum no longer determines the momentum of a neutrino since there are multiple ones. The
missing information in the four momenta makes the reconstruction of the di-tau mass $m_{\tau\tau}$
more challenging.

In the fully leptonic decay both taus decay only into leptons. This decay yields two neu-
trinos per tau, four in total. This system has the most unknown variables of all three
decays.

In the semileptonic decay only one tau decays leptonically, the other one decays hadron-
ically. This yields two neutrinos for the former and one for the latter.

The fully hadronic decay is the decay with the fewest unknown variables and also the one
that will later be analysed. Only two neutrinos are produced.

3.6.2 Background Events

The Higgs to di-tau (H$\to \tau\tau$) events cannot be fully separated from events such as a Z/γ^*
decaying into two taus ($Z/\gamma^* \to \tau\tau$). This background is largely irreducible and is much
larger than any signal originating from the Higgs decay.

3.6.3 Reconstruction of the Di-Tau Mass

The di-tau mass can be reconstructed in many different ways. The two most common, before the Missing Mass Calculator (MMC) technique was introduced, were the transverse mass method and the collinear approximation technique.
All equations are taken from [26] where a more thorough explanation can be found.

Transverse Mass Method

The transverse mass method only calculates a partial mass. For the calculations only the invariant mass of the visible decay products and the total missing energy $\not{E}_T$ are needed. For notational purposes the taus shall be labeled with a one and a two. The mass is defined as follows:

$$
\begin{aligned}
M_{\tau\tau}^2(\tau_{\mathrm{vis}_1}, \tau_{\mathrm{vis}_2}, \not{E}_T) = {} & m_{\mathrm{vis}_1}^2 + m_{\mathrm{vis}_2}^2 \\
& + 2\left(\sqrt{m_{\mathrm{vis}_1}^2 + p_{\mathrm{vis}_2}^2}\sqrt{m_{\mathrm{vis}_2}^2 + p_{\mathrm{vis}_1}^2} + \not{E}_T\sqrt{m_{\mathrm{vis}_1}^2 + p_{\mathrm{vis}_1}^2} + \not{E}_T\sqrt{m_{\mathrm{vis}_2}^2 + p_{\mathrm{vis}_2}^2}\right) \\
& - 2\left(\vec{p}_{\mathrm{vis}_1}\vec{p}_{\mathrm{vis}_2} + \vec{p}_{\mathrm{vis}_1}\not{E}_T + \vec{p}_{\mathrm{vis}_2}\not{E}_t\right)
\end{aligned}
$$

The momenta and missing invariant masses of the visible decay products are $\vec{p}_{\mathrm{vis}_{1,2}}$ and $m_{\mathrm{vis}_{1,2}}$ respectively. The missing transverse energy is $\vec{\not{E}}_T = (\not{E}_{T_x}, \not{E}_{T_y}, 0)$. This formula does not account for multiple neutrino momenta cancelling, thereby broadening the reconstructed mass of the di-tau system. The already very small signal is further washed into the background and becomes very hard to identify.

Collinear Approximation Technique

The collinear approximation reconstructs the mass based on the assumption that the neutrinos are nearly collinear with the remaining, visible decay products. In the approximation one also assumes that all energy lost is only due to neutrinos. For the collinear approximation the di-tau system has to be produced with a highly energetic jet. The mass can be calculated by solving the following equations:

$$
\not{E}_{T_x} = p_{\mathrm{mis}_1}\sin\theta_{\mathrm{vis}_1}\cos\phi_{\mathrm{vis}_1} + p_{\mathrm{mis}_2}\sin\theta_{\mathrm{vis}_2}\cos\phi_{\mathrm{vis}_2}
$$

and

$$
\not{E}_{T_y} = p_{\mathrm{mis}_1}\sin\theta_{\mathrm{vis}_1}\sin\phi_{\mathrm{vis}_1} + p_{\mathrm{mis}_2}\sin\theta_{\mathrm{vis}_2}\sin\phi_{\mathrm{vis}_2}
$$

With the same definition of $\not{E}_{T_x}$ and $\not{E}_{T_y}$ as in Section 3.6.3. The invisible momenta are p_{mis_1} and p_{mis_2}. The equations diverge for back to back tau production ($\phi_{\mathrm{vis}_1} = \phi_{\mathrm{vis}_2} + \pi$). The application of this approximation technique must therefore exclude back to back events. With the exclusion of such events one therefore gets for the mass:

$$m_{\tau\tau} = \frac{m_{\mathrm{vis}}}{\sqrt{x_1 x_2}}$$

with $x_{1,2} = p_{\mathrm{vis}_{1,2}}/(p_{\mathrm{vis}_{1,2}} + p_{\mathrm{mis}_{1,2}})$. The constraints of an energetic jet and no back to back events render the majority of di-tau events unsuitable for reconstruction. In addition, the collinear approximation is very sensitive to the accuracy of the missing energy measurement, often overestimating the mass. The overestimation leads to tails in the mass distribution.

Missing Mass Calculator Technique

The Missing Mass Calculator technique dispenses the assumptions of the collinear approximation but also reconstructs the mass, not merely the partial mass as in the transverse mass method. This technique can therefore be applied to all events and does not suffer the inaccuracies from working with a partial mass. There are almost no tails in the mass distribution with this technique.

Assuming no energy loss other than from the final state neutrinos in the di-tau decay of the Higgs boson one has 6 to 8 unknowns to solve for in only four equations. The unknowns are the spatial components of the invisible momentum carried away by the neutrinos for each tau lepton. One gets an additional unknown in the case of a leptonic decay, namely the invariant mass of the neutrinos from the leptonic decay. The equations available to determine the unknowns are as follows:

$$\not{E}_{T_x} = p_{\mathrm{mis}_1} \sin\theta_{\mathrm{mis}_1} \cos\phi_{\mathrm{mis}_1} + p_{\mathrm{mis}_2} \sin\theta_{\mathrm{mis}_2} \cos\phi_{\mathrm{mis}_2}$$

$$\not{E}_{T_y} = p_{\mathrm{mis}_1} \sin\theta_{\mathrm{mis}_1} \sin\phi_{\mathrm{mis}_1} + p_{\mathrm{mis}_2} \sin\theta_{\mathrm{mis}_2} \sin\phi_{\mathrm{mis}_2}$$

$$M_{\tau_1}^2 = m_{\mathrm{mis}_1}^2 + m_{\mathrm{vis}_1}^2 + 2\sqrt{m_{\mathrm{vis}_1}^2 + p_{\mathrm{vis}_1}^2}\sqrt{m_{\mathrm{mis}_1}^2 + p_{\mathrm{mis}_1}^2} - 2p_{\mathrm{vis}_1}^2 p_{\mathrm{mis}_1}^2 \cos\Delta\theta_{vm_1}$$

$$M_{\tau_2}^2 = m_{\mathrm{mis}_2}^2 + m_{\mathrm{vis}_2}^2 + 2\sqrt{m_{\mathrm{vis}_2}^2 + p_{\mathrm{vis}_2}^2}\sqrt{m_{\mathrm{mis}_2}^2 + p_{\mathrm{mis}_2}^2} - 2p_{\mathrm{vis}_2}^2 p_{\mathrm{mis}_2}^2 \cos\Delta\theta_{vm_2}$$

All variables are defined as in the previous two sections. The polar and azimuthal angles of the visible decay products are $\theta_{\mathrm{mis}_{1,2}}$ and $\phi_{\mathrm{mis}_{1,2}}$ accordingly. The system is still under-constrained. Using further knowledge of the kinematics introduces a likelihood for each

of the possible solutions. Depending on the decay channel of the tau one gets a two to four dimensional phase space of solutions. For a fully hadronic decay of the di-tau system the grid of solutions lies on $(\phi_{\mathrm{mis}_1}, \phi_{\mathrm{mis}_2})$. For a fully leptonic decay, one has $(\phi_{\mathrm{mis}_1}, \phi_{\mathrm{mis}_2}, m_{\mathrm{mis}_1}, m_{\mathrm{mis}_2})$. Weighting each point in this grid and choosing the most likely one, one can give an approximation of the di-tau mass. The MMC algorithm is trained on Z$\to \tau^+\tau^-$ templates.

4 Monte Carlo Generators

Monte Carlo event generators play an important role in today's high energy physics. The generators use the Monte Carlo algorithm to calculate physics processes. With the event generators one can simulate the expected behaviour of the colliding hadrons. The generator software is interfaced with the simulation software GEANT 4 [27, 28]. This software simulates our detector. The generators may deviate slightly from reality in their simulation of the physics processes and the detector, which is important to keep in mind. Monte Carlo generators are used to refine and prepare the analysis tools before they are applied to real data. In this thesis, simulated events stored in so called n-tuples are worked with[29].

4.1 POWHEG + PYTHIA 8

The events for the VBF and gg H$\to \tau^+\tau^-$ physics processes are simulated by the Monte Carlo generator POWHEG [30, 31] together with PYTHIA 8 [32]. POWHEG offers next-to-leading order (NLO) calculations of the Higgs boson productions in hard processes and PYTHIA 8 calculates the parton shower, the jet fragmentation and the underlying event as mentioned in 3.2.1. Together with GEANT 4 they simulate the proton-proton collisions and the interaction with the detector elements. One can not only extract the simulated detector data but also the truth information of the event, with truth meaning that no inaccuracies due to detector specific behavior are taken into account.
The data samples produced for the VBF, gg H$\to \tau^+\tau^-$ physics processes at $\sqrt{s} = 8\,\text{TeV}$ are listed in tables B.4 and B.5.

4.2 ALPGEN + JIMMY

The events for the Z$\to \tau^+\tau^-$ physics processes at $\sqrt{s} = 8\,\text{TeV}$ are simulated using the Monte Carlo generator ALPGEN [33–35] together with the JIMMY add on to the HERWIG program [36]. ALPGEN calculates the hard processes in hadronic collisions with an accuracy of leading order (LO) while HERWIG calculates the parton showers. The add on

JIMMY allows for multiple parton scattering events.

The data samples used for the Z boson decay are shown in tables B.1 to B.3. These data samples together with the Higgs boson data samples in tables B.4 and B.5 are the ones used in this thesis and will not be mentioned explicitly in the analysis section, but rather referred to by the physics process.

5 Event Reconstruction and Selection

In this chapter a look at the outline of the analysis program and the selection of reconstructed events will be taken. Not the exact programming but rather the general outline and selection criteria will be discussed. Kinematic and identification cuts are required to select good di-tau candidate events. The mass reconstruction algorithms are only run when the events satisfy certain selection cuts described in the following sections.

5.1 Event Selection

In the event selection, only di-tau events decaying hadronically are considered. Di-tau events are selected not only by their kinematic variables but also by identification (ID) cuts.

5.1.1 Tau Selection

Reconstruction Cuts

The first step in the reconstruction of hadronically decaying tau leptons is from clusters in the ECAL and HCAL. For tracks within a cone of $\Delta R < 0.2$ jets are associated to the tau candidate, with $\Delta R = \sqrt{(\Delta\phi)^2 + (\Delta\eta)^2}$. The transverse momentum is required to pass the threshold of $p_T > 20\,\text{GeV}$ and the pseudo-rapidity to fulfil $|\eta| < 2.5$. The transverse momentum threshold is introduced to avoid underlying event processes as explained in Section 3.2.1.

Identification Cuts

In addition to these kinematic cuts, identification cuts must be appliead. A requirement of the tau candidate being calorimeter seeded or calorimeter and the track seeded is intro-

duced. The number of tracks per tau candidate must be one or three. This cut is related to the decay topology of the tau, as explained in Section 3.5. It is required that the tau candidates have a charge of positive or negative one accordingly. Furthermore, the tau candidates must both pass the Jet/Sig BDT loose identification discriminant, where only one candidate is required to pass the Jet/Sig BDT medium identification discriminant. Here BDT refers to boosted decision trees which are an alternative method for particle identification in addition to neural networks [37]. This method generates scores for each event for e.g. the jet or electron identification. Tau candidates with a true muon veto or a true Electron BDT loose discriminant are neglected. In all those discriminants the term loose refers to how sensitive the cut is. Loose is the weakest option, followed by medium and then by tight. The option Electron BDT loose, for example, allows more events to pass and thereby also allows for more wrongly identified events than the option Electron BDT tight does. For tight very few events will pass but one is more certain that only electrons have passed the criterion.

At this stage the number of tau candidates that have passed the reconstruction and ID selection is required to be at least two. Events with less than two tau candidates passing the above criteria are not considered in the analysis.

5.1.2 Overlap Removal

As soon as the tau candidates are selected according to the kinematic and identification criteria mentioned above, all jets which geometrically match to those objects within $\Delta R < 0.2$ are removed and thus not considered in the analysis. This is often called overlap removal and assists into resolving possible object duplicates in the same event. Apart from the tau candidates some requirements are enforced upon the jets. The jets must, as the tau candidates, pass a transverse momentum threshold of $p_{T,\text{jet}} > 20\,\text{GeV}$ and must not have a pseudo-rapidity larger than $|\eta_{\text{jet}}| < 4.7$.

5.1.3 Truth Matching

In simulated events, the true information is also available and having access to the full particle history enables the possibility to match reconstructed objects to true particles. Checking if ΔR between the tau candidates and the visible truth information fulfils $\Delta R < 0.2$ yields the matched tau candidates. All cuts and their abbreviations are listed in Table B.6 in the order they occur in the analysis program.

5.1.4 Reconstruction Algorithms

Only events containing two tau candidates have been selected. It is assumed that one has a tau pair coming from either the Higgs boson or the Z boson. Reconstructing the mass of the di-tau system should yield the mass of the boson they originated from. For the Z one can easily probe the reconstruction methods because the Z mass is very well known. The boson is assumed to lie on its mass shell.

We can demand further requirements for the reconstruction. For the MMC algorithm the input parameters need to be mentioned.

If the MMC algorithm successfully reconstructed the di-tau kinematics and provided a solution, histograms can be filled with the kinematic variables of the MMC algorithm. For the algorithm to work as intended it is necessary that the fractions x_1 and x_2 lie between $0 < x_1, x_2 < 1$. This requirement is naturally connected to the requirement to have $\vec{E}_T$ bisecting the angle spanned by the two taus in the azimuthal plane. If this is the case one can fill further histograms and compare the results of events having passed the latter requirement and events with no further restriction. In Figures A.5 and A.6 the impact of this cut on the fractions x_1 and x_2 is shown. With this cut one removes most of the tail in the lower Higgs boson mass regime. Plots of the fraction x_1 drawn versus x_2 are pictured in Figures A.7, A.9 and A.11. No cuts on the fractions have been made in these plots.

To get an even deeper look into the properties of this algorithm one can require the missing energy to pass the $\not{E}_T > 20\,\text{GeV}$ criterion and one can exclude azimuthal angles that represent back to back events with $\Delta\varphi < \pi - \epsilon$, with ϵ small. Here, $\Delta\varphi$ is the difference in azimuthal angles of the two leading tau candidates and ϵ may be chosen to exclude as many back to back events and as little other events as possible.

MMC algorithm

For the MMC algorithm a few options were implemented. The options will not be explained here, since this would require a thorough walk through of the MMC class. Further information on the MMC algorithm can be found at [26]. These parameters are mentioned without explanation to enable a comparison between this and other studies of similar topics. The parameters are listed in Table B.7 with the corresponding value used to produce the data in the analysis in Chapter 6. I input the mass of the leading tau as $m_{\tau,\,\text{leading}} = 0.6\,\text{GeV}$ and set type0= 10 if the multiplicity of the leading tau is smaller or equal to two. The variable type refers to the kind of tau decay where type0 indicates the leading, type1 the sub-leading tau, meaning either 1-prong (type0=10) or 3-prong

(type0=30). For a multiplicity being larger than two $m_{\tau,\text{ leading}} = 1.2\,\text{GeV}$ and type0= 30 is set. For the sub-leading tau the same is done:

$$m_{\tau,\text{ sub-leading}} = 0.6 \quad \text{and} \quad \text{type1} = 10 \quad , \text{ for a multiplicity smaller than 3}$$
$$m_{\tau,\text{ sub-leading}} = 1.2 \quad \text{and} \quad \text{type1} = 30 \quad , \text{ for a multiplicity larger than 2}$$

With these parameters the di-tau mass is calculated with the MMC class.

As explained in 3.6.3, the fractions x_1 and x_2 are also derived for the MMC algorithm having the tau 4-momentum vectors calculated and the visible energy known. Plots of the fraction x_1 drawn against x_2 are shown in Figures A.8, A.10 and A.12.

5.2 Control Plots

The MMC results are cross-checked by looking at the distributions of different variables of the di-tau system. The behaviour of all the kinematic variables is well known, such as transverse momentum p_T, pseudo-rapidity η, azimuthal angle φ and angular distances $\Delta\varphi$, $\Delta\eta$ and ΔR, making them a good choice for probing our selection. In the process of writing the analysis program it is advisable to constantly check those plots for changes and anomalies. This has been done not only by myself but also by the supervisors and group members, yielding a broader view and a greater chance to spot possible mistakes. Many control plots are listed in the appendix A from Figure 5.1 to A.6 and two examples are shown in this section, namely Figures 5.1 and 5.2. The behaviour of all the kinematic variables in detail will not be explained, since that would leave no room for the actual analysis. For a thorough read through one might take a look at [1] or [38].

While working on the analysis program one can check for those kinematic variables. For example in Figure 5.1 the cosine of the angle between the two tau candidates $\cos(\alpha)$ is plotted. It is expected to be evenly distributed with a shift towards back to back events, as can be seen in the histogram. Checking the difference in pseudo-rapidities $\Delta\eta$ in A.1, in the azimuthal angle $\Delta\varphi$ in A.2 or in the distance $\Delta R = \sqrt{(\Delta\varphi)^2 + (\Delta\eta)^2}$, in Figure A.3, looks sensible as well.

It is interesting to take a look at the momentum distribution of the leading and the sub-leading tau candidates. In Figures 5.2 and A.4 the transverse momenta for the two leading tau candidates are illustrated. The transverse momentum of the sub-leading tau candidate is distributed at lower values, as expected.
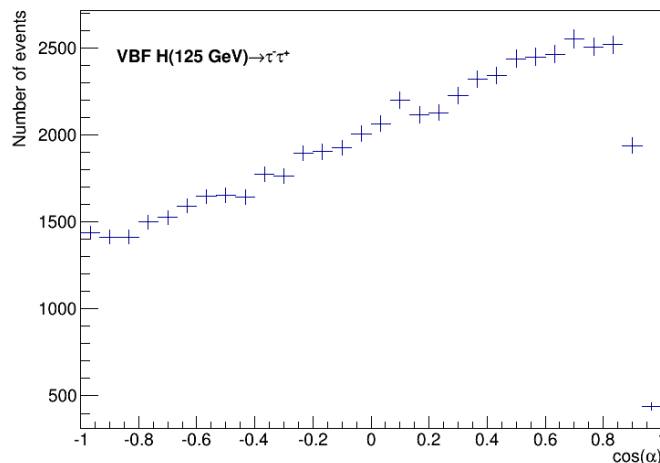
Figure 5.1: The $\cos(\alpha)$ between the two leading tau candidates, where α is the three dimensional angle between the momentum vectors of the two taus. The events for the VBF H$\to$ $\tau^-\tau^+$ physics process with $m_H = 125$ GeV at $\sqrt{s} = 8$ TeV are simulated using the POWHEG + PYTHIA 8 Monte Carlo generator. Events are required to fulfil the selection cuts as described in Section 5.3, listed in Table B.8.

5.3 Event Cut Flow

For a better understanding of all the plots, monitoring of the cut stage at which the histogram was filled is necessary. Even though each caption includes some information about the cuts applied in the corresponding plot an overview is very helpful. In Table B.8 histograms and the cuts applied before filling each histogram are listed. All mass distributions have a bin width of 5 GeV. The cuts are named according to Table B.6.

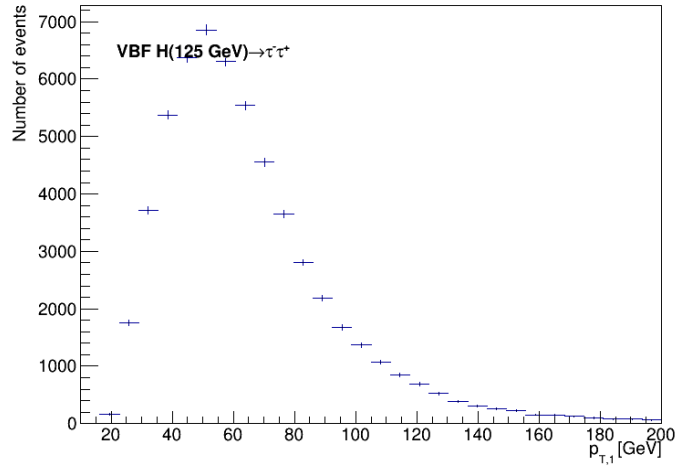***Figure 5.2:*** The transverse momentum of the leading tau candidate. The events for the VBF H→ $\tau^-\tau^+$ physics process with $m_H = 125\,\text{GeV}$ at $\sqrt{s} = 8\,\text{TeV}$ are simulated using the POWHEG + PYTHIA 8 Monte Carlo generator. Events are required to fulfil the selection cuts as described in Section 5.3, listed in Table B.8.

6 Results and Analysis

In this chapter the data gathered by the selection criteria and the application of the reconstruction techniques on the Monte Carlo data samples listed in tables B.1 to B.5 is analysed. To start off, a comparison between the two reconstruction methods applied to data samples for VBF H$\to \tau^+\tau^-$ and gg H$\to \tau^+\tau^-$ physics processes with $m_H = 125\,\mathrm{GeV}$ is made. Afterwards, the behaviour of the MMC algorithm is looked at. Its behaviour is probed for different physics processes, namely the VBF, gg H$\to \tau^+\tau^-$ and Z$\to \tau^+\tau^-$. Next the performance of the MMC algorithm on different Higgs boson masses for $m_H = 120, 125, 135, 145\,\mathrm{GeV}$ is tested. Finally, a brief look at the influence of the number of charged tracks in the di-tau decay on the MMC algorithm is taken.

6.1 Mass Reconstruction Techniques in Comparison

In this section the mass reconstruction techniques applied to VBF, gg H$\to \tau^+\tau^-$ data samples for $m_H = 125\,\mathrm{GeV}$ is compared.

6.1.1 Gaussian Fit of Core Distributions

The core distributions of the two mass distributions from the MMC algorithm and the collinear approximation are fit with a Gaussian function as defined below:

$$f_{\mathrm{fit}} = a \cdot \exp\left(-\frac{1}{2}\left(\frac{x - \mu}{\sigma'}\right)^2\right) \tag{6.1}$$

with fit parameters a, μ and σ'. The parameter μ yields the mean of the Gaussian and thus the peak position of the mass distribution. The standard deviation of the Gaussian function is given by σ'. The histogram for the Gaussian function fit to the VBF data sample is illustrated in Figure 6.1 and the Gaussian fit to the gg data sample is shown in Figure 6.2. The fit parameters for both data samples are listed in Table B.9 and Table B.10 accordingly. The errors of the fit parameters are not mentioned here, since the

choice of the core distribution was made by eye and is therefore somewhat arbitrary. This systematic error is assumed to be larger than the statistical one given in the tables.

In both histograms the mass distribution for the collinear approximation shows the properties as discussed in Section 3.6.3. The tail towards higher masses is relatively large. On the contrary, the mass distribution estimated by the MMC technique is much sharper and shows almost no tails, as predicted in Section 3.6.3. The fit paramters for the VBF data tell a different story. The standard deviation of the Gaussian functions is roughly the same for the collinear approximation as for the MMC algorithm with a value of $\sigma' \approx 23\,\text{GeV}$. This might be due to a poor choice of the core distribution. For the gg data sample the standard deviation of the collinear approximation $\sigma'_{\text{Coll}} \approx 30\,\text{GeV}$ is notably worse than for the MMC technique with $\sigma' \approx 25\,\text{GeV}$. Another prediction made in Section 3.6.3 is the shift of the peak position in the mass distribution for the collinear approximation. The Higgs boson mass, as produced by the Monte Carlo generators, is set to be $m_H = 125\,\text{GeV}$ for both the VBF and gg data samples. In both cases the mass is shifted to $\mu \approx 137\,\text{GeV}$ for the VBF sample and to $\mu \approx 140\,\text{GeV}$ for the gg sample for the collinear approximation. The peak position for the mass approximated by the MMC technique is shifted in the opposite direction. For the VBF sample the peak is at $\mu \approx 114\,\text{GeV}$ and for the gg data sample at $\mu \approx 109\,\text{GeV}$. The mean of the mass distribution as estimated by the MMC does not necessarily have to be exactly at the input mass point, since the algorithm was tuned using $Z \rightarrow \tau^+\tau^-$ templates. Different MMC versions lead to different outputs because they are differently tuned. Overall, the mean and width of the mass distribution is very sensitive to the MMC version and setup.

6.1.2 Efficiencies of the Mass Reconstruction Techniques

The two mass reconstruction techniques need not only be compared in the accuracy but also in the efficiency. The efficiency is determined by the number of events used to calculate the reconstructed mass over the number of events passing the reconstruction cuts C_{default}, as listed in Table B.6. This fraction yields an efficiency which is listed in percentages for all data samples in Table B.11. The number of events that are used in the reconstruction techniques is constrained by the requirement $0 < x_1, x_2 < 1$. For both algorithms the fractions x_1 and x_2 are defined in the Section 3.6.3.

For the MMC algorithm one expects a greater number of events being used than for the collinear approximation, since the requirement of almost back to back tau pairs and high energetic jets were dropped. The analysis code stores both, jets with a multiplicity of zero and events with no jets at all passing the cut criterion, in the bin of zero multiplicity. The percentage of jets with a multiplicity of zero passing a requirement of a minimum
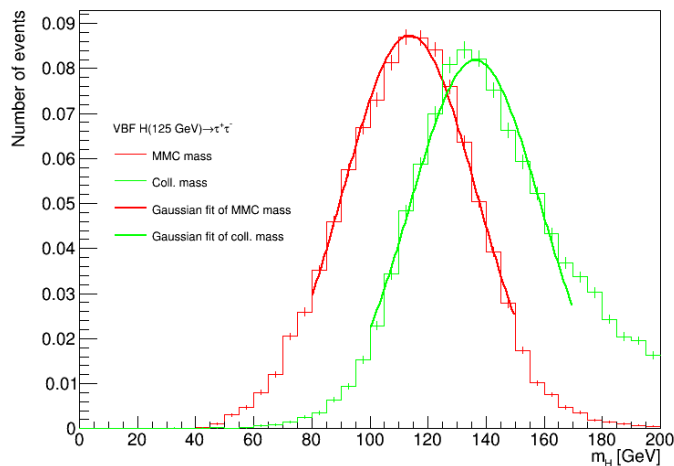
Figure 6.1: Di-tau mass distributions calculated with the MMC algorithm and with the collinear approximation method, normalized to unit area. The core distributions are fit with a Gaussian function. The fitting results are illustrated in B.9. The events for the VBF H$\to \tau^-\tau^+$ physics process with $m_H = 125$ GeV at $\sqrt{s} = 8$ TeV are simulated using the POWHEG + PYTHIA 8 Monte Carlo generator. Events are required to fulfil the selection cuts as described in Section 5.3, listed in Table B.8.

Figure 6.2: Di-tau mass distributions calculated with the MMC algorithm and with the collinear approximation method, normalized to unit area. The core distributions are fit with a Gaussian function. The fitting results are illustrated in B.10 The events for the gg H$\to \tau^-\tau^+$ physics process with $m_H = 125$ GeV at $\sqrt{s} = 8$ TeV are simulated using the POWHEG + PYTHIA 8 Monte Carlo generator. Events are required to fulfil the selection cuts as described in Section 5.3, listed in Table B.8.
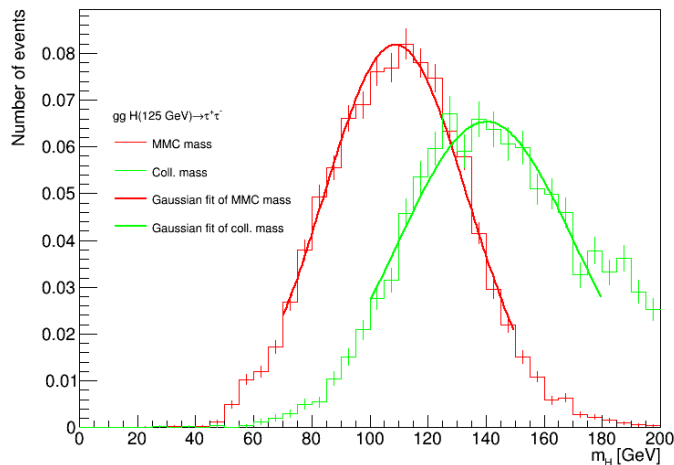
transverse momentum of $p_{T,\text{jet}} > 20\,\text{GeV}$ is $2.15\,\%$ and the number of jets passing $p_{T,\text{jet}} > 25\,\text{GeV}$ is $4.65\,\%$ of the events passing the default cut $\text{C}_{\text{default}}$. Therefore, the events cut away with the transverse momentum requirement for the jets must be less than $2.15\,\%$ or $4.65\,\%$ accordingly.

The numbers given above yield a minimum efficiency of the collinear approximation of $57.34\,\%$ for the $p_T > 20\,\text{GeV}$ cut or $54.84\,\%$ for the $p_T > 25\,\text{GeV}$ cut. The efficiency as calculated without the $p_{T,\text{jet}}$ cut is $59.49\,\%$. With an applied $p_{T,\text{jet}}$ cut, one can see the corrections are within a few percent or smaller.

6.2 Dependence of the MMC Algorithm on the Physics Process

This section covers the impact of the physics process on the di-tau mass reconstruction via the MMC method. It look at the Higgs boson and the Z boson decaying into tau pairs is taken. The two different Higgs production channels, the VBF and the gg are looked at.

VBF H$\to \tau^- \tau^+$ compared to Z$\to \tau^- \tau^+$

Firstly, a look at the VBF H$\to \tau^- \tau^+$ physics process compared to the Z$\to \tau^- \tau^+$ process is taken. In Figure 6.3 the mass distributions calculated with the MMC algorithm are illustrated. The mass distribution of the Higgs boson with a much higher mass is expected to be broader than the one of the Z boson. This behaviour can be understood as follows. The Higgs boson being a more massive particle than the Z boson, its decay products, including the neutrino, are therefore expected to be emitted with higher energies. But it is known that the resolution of E_T^{mis} degrades as $\sum E_T$ of the event increases as described in the following formula:

$$\frac{\sigma'(E_T^{\text{mis}})}{E_T} \propto k \frac{1}{\sqrt{\sum E_T}}$$

where $\sum E_T$ is the scalar sum of all transverse momenta of the reconstructed objects in the event and k is a characteristic constant of the process in question. Therefore, the mass resolution is significantly affected by the resolution of E_T^{mis}. This dependence yields a broader curve for a higher energy and since the Higgs boson is heaver than the Z boson more energy is needed for the production and will later be detected in the calorimeter.

In the mass distribution of the Z$\to \tau^+ \tau^-$, such as in Figure 6.3, one also observes the exis-

tence of a tail at the right-hand side of the distribution. The distributions of the difference in the pseudo-rapidity $\Delta\eta$ as well as the distributions for the difference in the azimuthal angle $\Delta\varphi$ plotted against the mass distribution do not show any significant distinctions between the Higgs boson and the Z boson decays. The plots of the pseudo-rapidity can be found in Figures A.16, A.20 and A.23. The histograms of ΔR are illustrated in A.14, A.18 and A.22. The histograms are further explained in section 6.5.

Figure 6.3: Di-tau mass distributions calculated with the MMC algorithm for two different physics processes, normalized to unit area. The events for the VBF H$\to \tau^-\tau^+$ physics process with $m_H = 125\,\text{GeV}$ at $\sqrt{s} = 8\,\text{TeV}$ are simulated using the POWHEG + PYTHIA 8 Monte Carlo generator. The events for the Z$\to \tau^-\tau^+$ physics process at $\sqrt{s} = 8\,\text{TeV}$ are simulated using the ALPGEN +JIMMY Monte Carlo generator. Events are required to fulfil the selection cuts as described in Section 5.3, listed in Table B.8.

gg H$\to \tau^-\tau^+$ compared to Z$\to \tau^-\tau^+$

Comparing the gg H$\to \tau^-\tau^+$ physics process with the Z$\to \tau^-\tau^+$ physics process yields the same distinction and features as explained above. The comparison is illustrated in Figure 6.4.

VBF H$\to \tau^-\tau^+$ compared to gg H$\to \tau^-\tau^+$

The two decays of the through VBF produced Higgs boson and the through gg produced Higgs boson should result in similar mass distributions of the tau pair. Contrary to this prediction the two histograms show discrepancies. The peak of the mass distribution for gg H$\to \tau^-\tau^+$ seems to be shifted slightly towards a lower Higgs boson mass than the
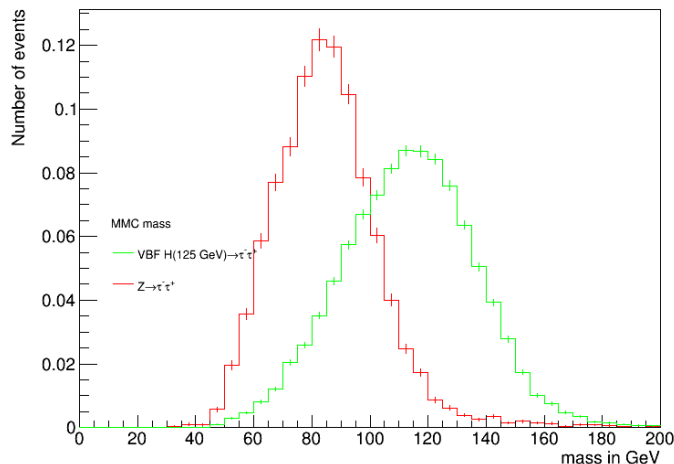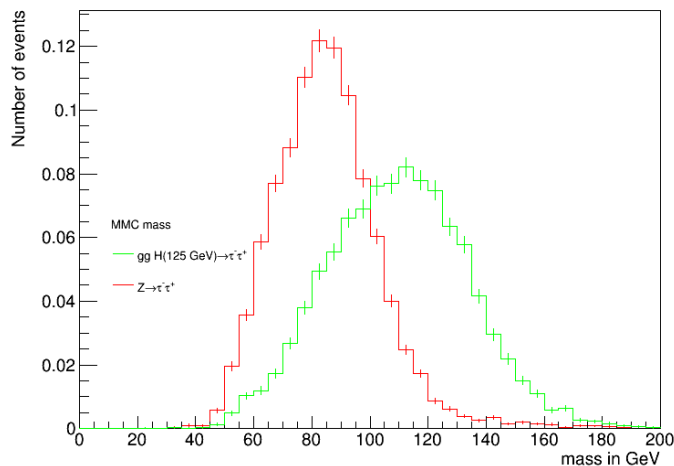
35

Figure 6.4: Di-tau mass distributions calculated with the MMC algorithm for two different physics processes, normalized to unit area. The events for the VBF H→ $\tau^-\tau^+$ physics process with $m_H = 125\,\text{GeV}$ at $\sqrt{s} = 8\,\text{TeV}$ are simulated using the POWHEG + PYTHIA 8 Monte Carlo generator. The events for the Z→ $\tau^-\tau^+$ physics process at $\sqrt{s} = 8\,\text{TeV}$ are simulated using the ALPGEN +JIMMY Monte Carlo generator. Events are required to fulfil the selection cuts as described in Section 5.3, listed in Table B.8.

peak of the mass distribution for VBF H→ $\tau^-\tau^+$. Another distinction between the two histograms can be made in the width. Since the mass distribution for VBF peaks at a higher number of events one can directly conclude that its width is smaller, since both histograms are normalized and can be assumed to have a Gaussian shape.

The reasoning for this behaviour may be found when inspecting the Monte Carlo generator more closely. An increase in statistics, as there is in the VBF data sample compared to the gg data sample, does not sharpen the distribution and is thereby no explanation for this behaviour.

6.3 Dependence of the MMC Algorithm on the Higgs Mass

Even though the Higgs boson mass is relatively accurately measured by now, one still wants to know how a different hypothetical mass can influence the algorithm to better understand its behaviour. Different Higgs mass hypotheses with $m_H = 120, 125, 135, 145\,\text{GeV}$ are tested in this section.

As explained in Section 6.1 a higher energy particle should yield a broader mass distri-
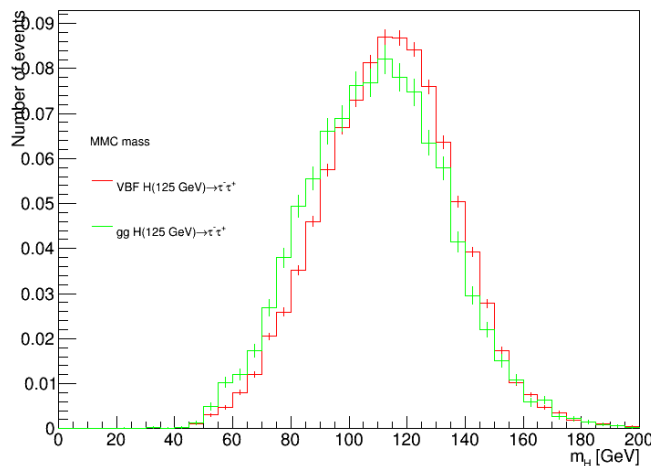
Figure 6.5: Di-tau mass distributions calculated with the MMC algorithm for two different physics processes, normalized to unit area. The events for the VBF and gg H$\to \tau^- \tau^+$ physics process with $m_H = 125\,\text{GeV}$ at $\sqrt{s} = 8\,\text{TeV}$ are simulated using the POWHEG + PYTHIA 8 Monte Carlo generator. Events are required to fulfil the selection cuts as described in Section 5.3, listed in Table B.8.

bution than a less energetic particle. For different Higgs boson masses one deals with differences in the energy. The resolution scales with the mass, meaning the higher the mass, the broader is the mass distribution, as is explained in Section 6.2. This behaviour can be observed in Figure 6.6 where four different samples of the VBF H$\to \tau^+ \tau^-$ with $m_H = 120, 125, 135, 145\,\text{GeV}$ have been plotted. The plot has been generated after the application of all cuts, namely C$_{\text{all}}$, as shown in Table B.6. With the bare eye no change in shape can be recognized.

The MMC algorithm reconstructs the different Higgs boson masses at the right place with reasonably good width.

6.4 Dependence of the MMC Algorithm on the Number of Tracks

The dependence and performance of the MMC calculation on the number tau tracks is studied in this section for VBF, gg H$\to \tau^+ \tau^-$ data samples with $m_H = 125\,\text{GeV}$.

In Figures 6.7 and 6.8 the mass distributions, estimated with the MMC algorithm is illustrated for the VBF and gg Higgs boson production, correspondingly. For the creation of the two plots a different number of events has been input into the analysis program.
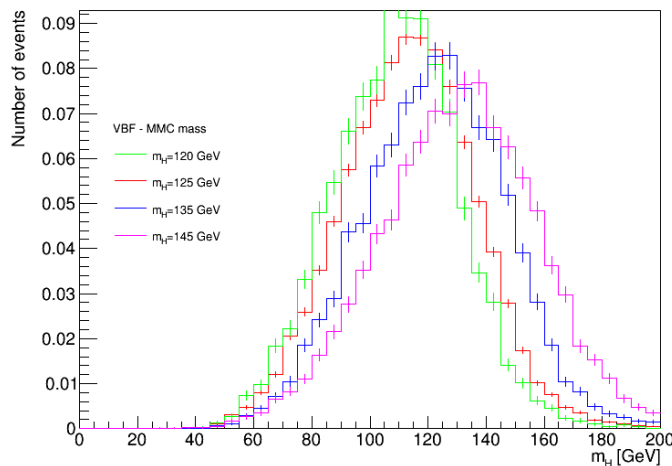
Figure 6.6: Di-tau mass distributions calculated with the MMC algorithm for $m_H = 120, 125, 135, 145\,\text{GeV}$, normalized to unit area. Simulated events using the POWHEG + PYTHIA 8 Monte Carlo generator for the VBF H$\to \tau^- \tau^+$ physics process at $\sqrt{s} = 8\,\text{TeV}$. Events are required to fulfil the selection cuts as described in Section 5.3, listed in Table B.8.

For the VBF process about 300,000 events were considered of which only 58,000 met the selection criteria. For the gg process 100,000 events were considered of which about 14,000 met the selection criteria. The different numbers of events input implies a greater statistical fluctuation for the gg sample. The normalization does not have any impact this behaviour. The number of events where both taus decay with three charged tracks, in the plot marked as 3-3 prong, is even lower and one can clearly see the fluctuation increase in Figure 6.8 compared to Figure 6.7.

Given the statistics of the simulated samples, one cannot draw any safe conclusion on the impact of the number of tracks on the di-tau mass reconstruction. In these two data samples it looks as if the number of tracks does not influence the algorithm, but the histograms clearly show large statistical fluctuations. For a definite answer even more data samples would be needed.

6.5 MMC Mass Dependency on Kinematic Quantities

In this section a brief look at the dependency of the MMC algorithm on di-tau kinematic quantities, such as $\Delta\eta$, $\Delta\varphi$ and more, is taken. The plots for each quantity are given for the three different physics processes as mentioned for example in Chapter 4.
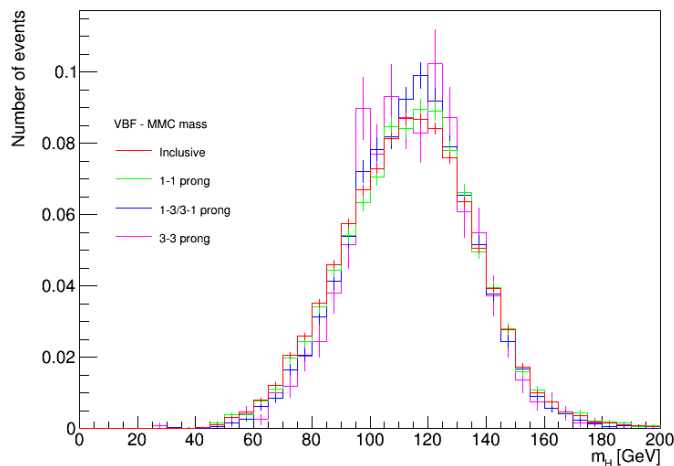
Figure 6.7: Di-tau mass distributions calculated with the MMC algorithm. Distributions are shown for different combinations of tau-pairs having a different number of charged tracks, normalized to unit area. The events for the VBF H$\rightarrow \tau^-\tau^+$ physics process with $m_H = 125$ GeV at $\sqrt{s} = 8$ TeV are simulated using the POWHEG + PYTHIA 8 Monte Carlo generator. Events are required to fulfil the selection cuts as described in Section 5.3, listed in Table B.8.

Figure 6.8: Di-tau mass distributions calculated with the MMC algorithm. Distributions are shown for different combinations of tau-pairs having a different number of charged tracks, normalized to unit area The events for the gg H$\rightarrow \tau^-\tau^+$ physics process with $m_H = 125$ GeV at $\sqrt{s} = 8$ TeV are simulated using the POWHEG + PYTHIA 8 Monte Carlo generator. Events are required to fulfil the selection cuts as described in Section 5.3, listed in Table B.8.
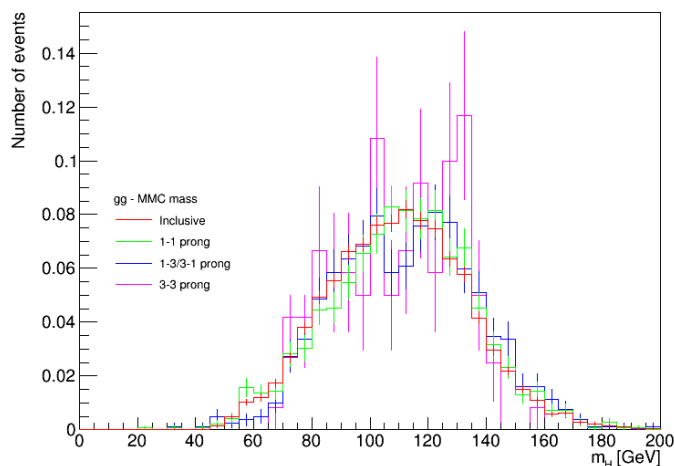
To begin with the mass distribution plotted against $\Delta\varphi$ in Figures A.15 and A.19 is inspected. The scatter plot shows an even distribution with a slight shift towards back to back events. This shift is only noticeable in $\Delta\varphi$ but has no impact on the mass. No difference between the physics processes can be found.

I find the same result for the mass distribution plotted against $\cos(\alpha)$ in figures A.17 and A.21. Again one has a uniform distribution with a slight shift towards back to back events.

The scatter plots of $\Delta\eta$ in figures A.16, A.20 and A.23 show the behaviour as expected from Section 5.2. Plotting the distance ΔR against the mass distribution in figures A.14, A.18 and A.22 yields the from Section 5.2 expected results. The histograms for the Z boson decay shown in A.23 and A.22 was created by adding the data samples listed in tables B.1 to B.3 with a weight of σ/N. Here σ is the cross section and N the number of events passing the default cut C_{default}. The cross sections are listed in the same tables as the data samples. The histogram was also normalized.

Additionally in A.13 the transverse momentum of the resonance Lorentz vector from the MMC algorithm is plotted. The p_T distribution is a characteristic of the Higgs boson. Summing up one can state that the MMC algorithm is well behaved in respect to all tested kinematic quantities.

7 Conclusions

The observation of the Higgs boson coupling to fermions would confirm the prediction by the SM. Working towards this goal in this thesis the results are summarised in the following.

The tau lepton decay channels can be divided into three kinds, the purely leptonic, the 1-prong hadronic and the 3-prong hadronic decay. All of the decays include at least one neutrino. Since the di-tau system is the one of interest, a mass reconstruction technique is required. The techniques studied are the collinear approximation as well as the MMC algorithm. The former is the currently used technique. The latter is a technique with promising new features which ought to be explored in this thesis. Both methods were explained in Section 3.6.3. The analysis of the discrepancies between the two reconstruction methods led us through a comparison of the two techniques on the same data samples in Section 6.1. The comparison uncovered sharper mass distributions for the MMC algorithm, making them more distinguishable from background than the distribution of the collinear approximation with its large tail in large mass regions. The physics process did not have a notable influence on the performance of the MMC algorithm apart from what was expected. The same positive result could be found when analysing the impact of the Higgs boson mass on the performance of the algorithm. The mass does not degrade the MMC calculation performance but only yields expected deviations independent of the MMC algorithm. The study of the influence of the number of tracks did not yield any results due to large statistical fluctuations in the histograms. Furthermore, the MMC algorithm's efficiency was evaluated, which proved to be roughly the same as for the collinear approximation, contrary to what was predicted in Section 3.6.3.

In summary, the MMC algorithm is a promising tool in the analysing the coupling of the Higgs boson to fermions, namely the tau leptons. The resolution in the mass distribution is much better for the MMC algorithm in comparison to the collinear approximation. The improved resolution is due to the lack of tails in the higher mass regimes.

Further studies with more data samples could yield more definite results, not wanting to dilute the already satisfying results. The next step will be the application of the MMC algorithm to the new data from RunII of the Lhc. This will hopefully yield proof of the

coupling between the Higgs boson and fermions.

A Additional Plots

The histograms in this chapter are all taken from the VBF H$\to \tau^-\tau^+$ physics process data sample. They are merely included to illustrate the procedure of writing an analysis program and look alike for the other processes.

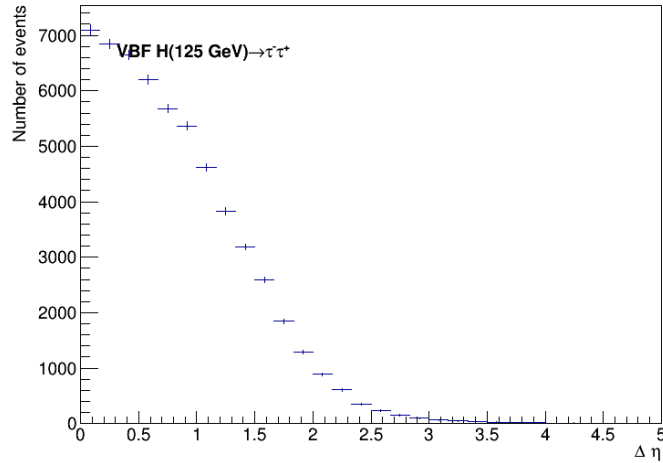*Figure A.1:* The difference of the pseudo-rapidity $\Delta\eta$ between the two leading tau candidates. The events for the VBF H$\to \tau^-\tau^+$ physics process with $m_H = 125\,\mathrm{GeV}$ at $\sqrt{s} = 8\,\mathrm{TeV}$ are simulated using the POWHEG + PYTHIA 8 Monte Carlo generator. Events are required to fulfil the selection cuts as described in Section 5.3, listed in Table B.8.

Figure A.2: The difference of azimuthal angle $\Delta\eta$ between the two leading tau candidates. The events for the VBF H$\to \tau^-\tau^+$ physics process with $m_H = 125$ GeV at $\sqrt{s} = 8$ TeV are simulated using the POWHEG + PYTHIA 8 Monte Carlo generator. Events are required to fulfil the selection cuts as described in Section 5.3, listed in Table B.8.
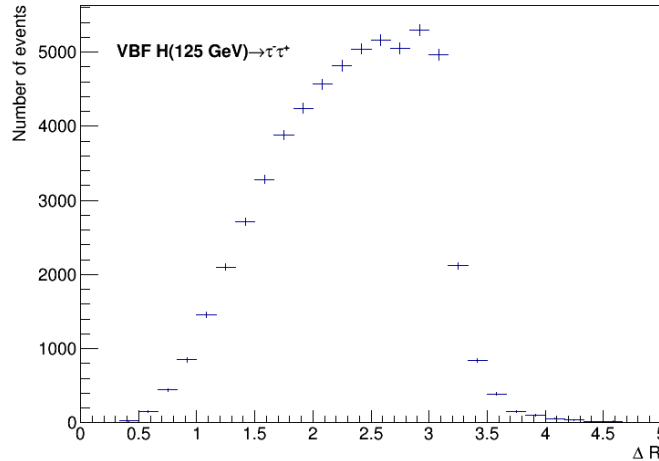
Figure A.3: The difference in the distance ΔR between the two leading tau candidates. The events for the VBF H$\to \tau^-\tau^+$ physics process with $m_H = 125$ GeV at $\sqrt{s} = 8$ TeV are simulated using the POWHEG + PYTHIA 8 Monte Carlo generator. Events are required to fulfil the selection cuts as described in Section 5.3, listed in Table B.8.
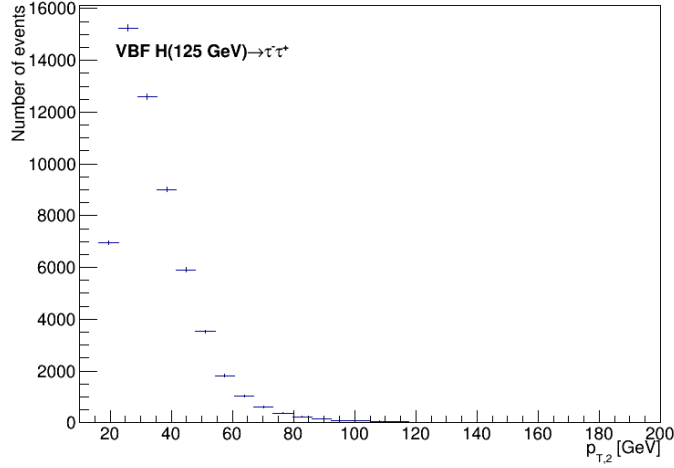
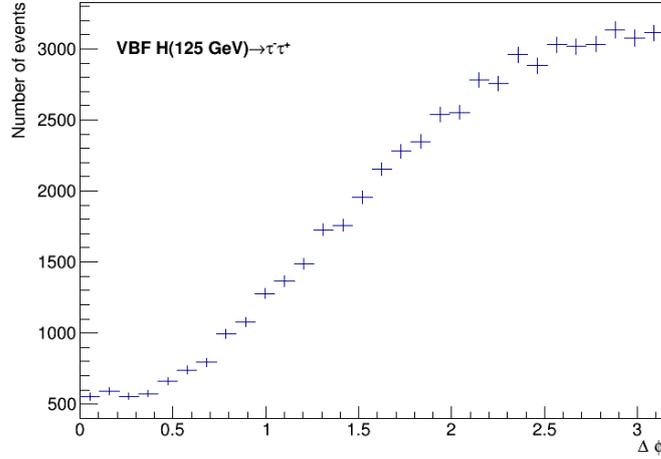***Figure A.4:*** The transverse momentum of the sub-leading tau candidate. The events for the VBF H→ $\tau^-\tau^+$ physics process with $m_H = 125\,\text{GeV}$ at $\sqrt{s} = 8\,\text{TeV}$ are simulated using the POWHEG + PYTHIA 8 Monte Carlo generator. Events are required to fulfil the selection cuts as described in Section 5.3, listed in Table B.8.
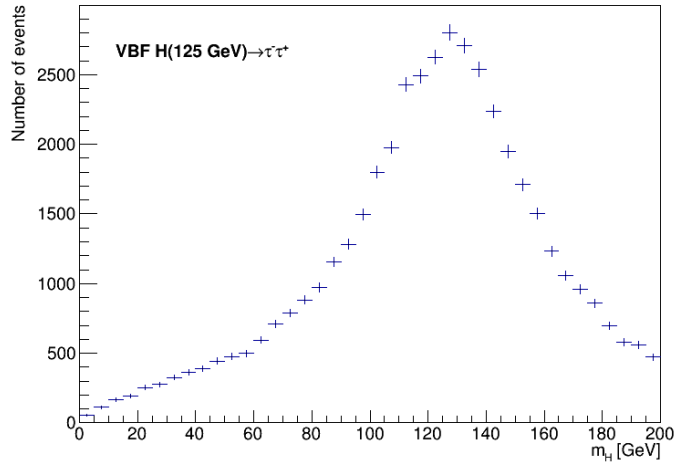
Figure A.5: The mass distribution calculated with the collinear approximation with no requirement on the fractions x_1 and x_2. The events for the VBF H→ $\tau^-\tau^+$ physics process with $m_H = 125\,\text{GeV}$ at $\sqrt{s} = 8\,\text{TeV}$ are simulated using the POWHEG + PYTHIA 8 Monte Carlo generator. Events are required to fulfil the selection cuts as described in Section 5.3, listed in Table B.8.

45

Figure A.6: The mass distribution calculated with the collinear approximation with the requirement on the fractions to be $0 < x_1, x_2 < 1$. The events for the VBF H$\to \tau^-\tau^+$ physics process with $m_H = 125$ GeV at $\sqrt{s} = 8$ TeV are simulated using the POWHEG + PYTHIA 8 Monte Carlo generator. Events are required to fulfil the selection cuts as described in Section 5.3, listed in Table B.8.


Figure A.7: Fractions x_1 and x_2 of the hadronic tau visible momentum defined as $x_i = p_{T,i,vis}/p_{T,i,true}$ in the collinear approximation are shown. The events for the VBF H$\to \tau^-\tau^+$ physics process with $m_H = 125$ GeV at $\sqrt{s} = 8$ TeV are simulated using the POWHEG + PYTHIA 8 Monte Carlo generator. Events are required to fulfil the selection cuts as described in Section 5.3, listed in Table B.8.

Figure A.8: Fractions x_1 and x_2 of the hadronic tau visible momentum defined as $x_i = p_{T,i,vis}/p_{T,i,true}$ in the MMC algorithm are shown. The events for the VBF H$\to \tau^- \tau^+$ physics process with $m_H = 125\,\text{GeV}$ at $\sqrt{s} = 8\,\text{TeV}$ are simulated using the POWHEG + PYTHIA 8 Monte Carlo generator. Events are required to fulfil the selection cuts as described in Section 5.3, listed in Table B.8.
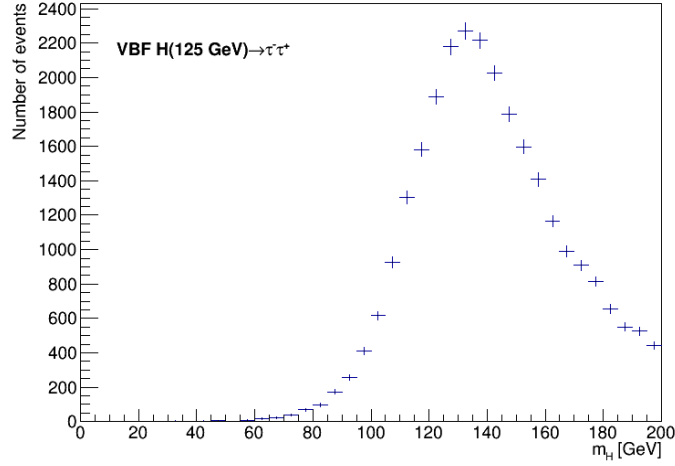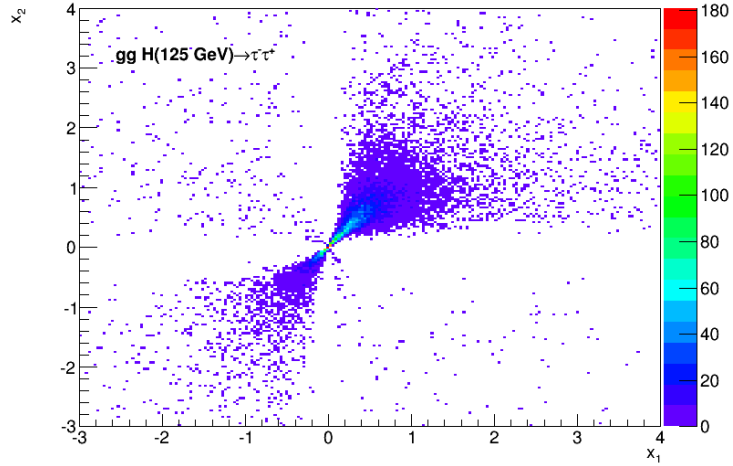

Figure A.9: Fractions x_1 and x_2 of the hadronic tau visible momentum defined as $x_i = p_{T,i,vis}/p_{T,i,true}$ in the collinear approximation are shown. The events for the gg H$\to \tau^- \tau^+$ physics process with $m_H = 125\,\text{GeV}$ at $\sqrt{s} = 8\,\text{TeV}$ are simulated using the POWHEG + PYTHIA 8 Monte Carlo generator. Events are required to fulfil the selection cuts as described in Section 5.3, listed in Table B.8.
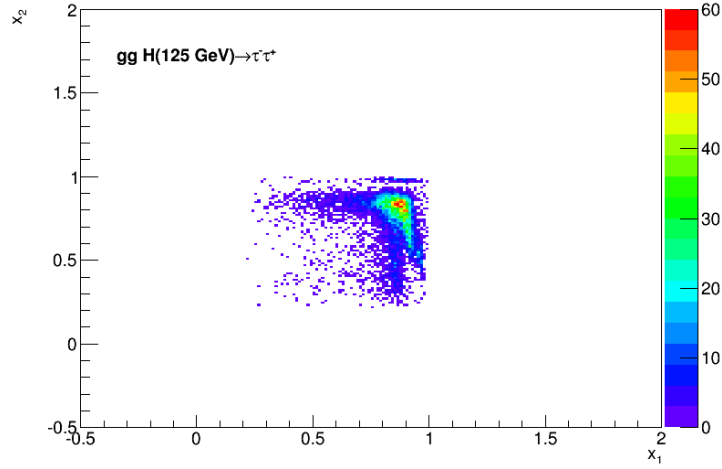
Figure A.10: Fractions x_1 and x_2 of the hadronic tau visible momentum defined as $x_i = p_{T,i,vis}/p_{T,i,true}$ in the MMC algorithm are shown The events for the gg H$\rightarrow \tau^- \tau^+$ physics process with $m_H = 125\,\text{GeV}$ at $\sqrt{s} = 8\,\text{TeV}$ are simulated using the POWHEG + PYTHIA 8 Monte Carlo generator. Events are required to fulfil the selection cuts as described in Section 5.3, listed in Table B.8.
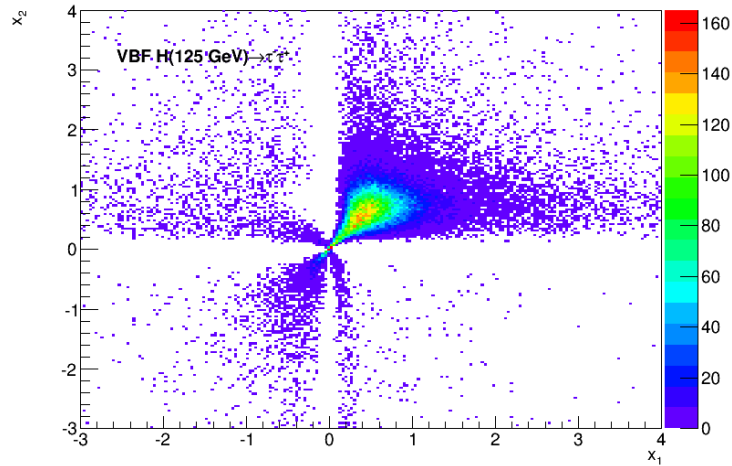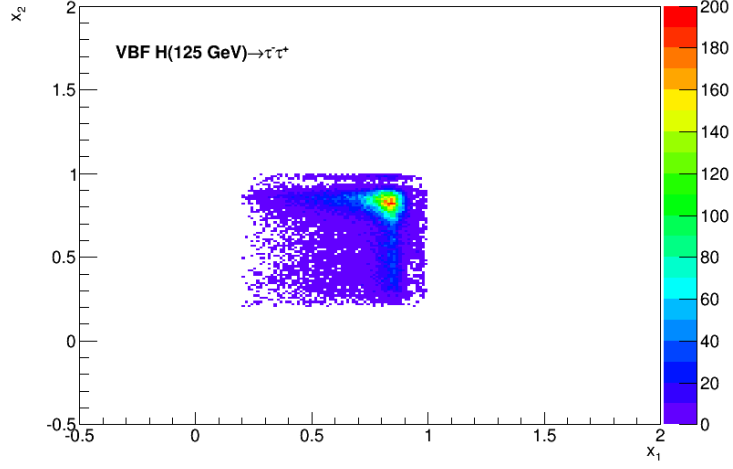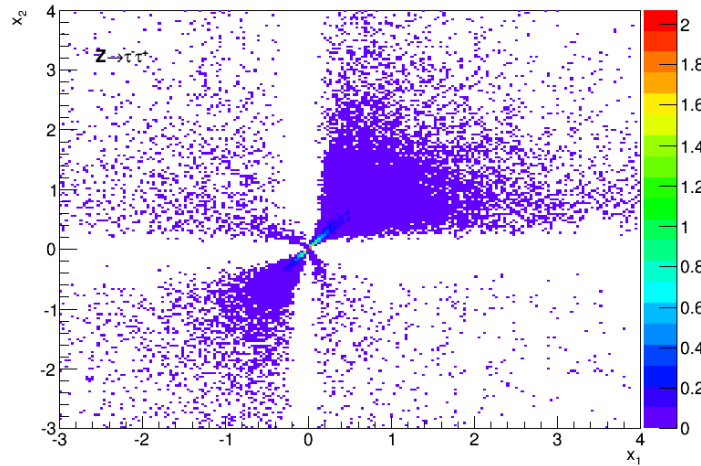

Figure A.11: Fractions x_1 and x_2 of the hadronic tau visible momentum defined as $x_i = p_{T,i,vis}/p_{T,i,true}$ in the collinear approximation are shown. The events for the Z$\rightarrow \tau^- \tau^+$ physics process at $\sqrt{s} = 8\,\text{TeV}$ are simulated using the ALPGEN +JIMMY Monte Carlo generator. Events are required to fulfil the selection cuts as described in Section 5.3, listed in Table B.8.
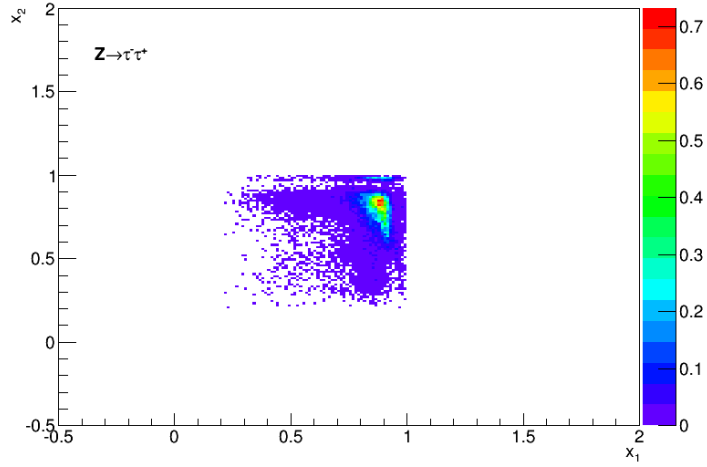
Figure A.12: Fractions x_1 and x_2 of the hadronic tau visible momentum defined as $x_i = p_{T,i,vis}/p_{T,i,true}$ in the MMC algorithm are shown The events for the Z$\to \tau^-\tau^+$ physics process at $\sqrt{s} = 8\,\text{TeV}$ are simulated using the ALPGEN +JIMMY Monte Carlo generator. Events are required to fulfil the selection cuts as described in Section 5.3, listed in Table B.8.

Figure A.13: The transverse momentum p_T of the resonance from the MMC algorithm. The events for the VBF H$\to \tau^-\tau^+$ physics process with $m_H = 125\,\text{GeV}$ at $\sqrt{s} = 8\,\text{TeV}$ are simulated using the POWHEG + PYTHIA 8 Monte Carlo generator. Events are required to fulfil the selection cuts as described in Section 5.3, listed in Table B.8.

***Figure A.14:*** The variable ΔR between the leading and sub-leading tau is plotted against the di-tau mass approximated by the MMC algorithm, normalized to unit area. The events for the VBF H$\rightarrow \tau^-\tau^+$ physics process with $m_H = 125$ GeV at $\sqrt{s} = 8$ TeV are simulated using the POWHEG + PYTHIA 8 Monte Carlo generator. Events are required to fulfil the selection cuts as described in Section 5.3, listed in Table B.8.

Figure A.15: The difference of the azimuthal angle $\Delta\phi$ between the leading and sub-leading tau is plotted against the di-tau mass approximated by the MMC algorithm, normalized to unit area. The events for the VBF H$\rightarrow \tau^-\tau^+$ physics process with $m_H = 125$ GeV at $\sqrt{s} = 8$ TeV are simulated using the POWHEG + PYTHIA 8 Monte Carlo generator. Events are required to fulfil the selection cuts as described in Section 5.3, listed in Table B.8.

Figure A.16: The difference of the pseudo-rapidity $\Delta\eta$ between the leading and sub-leading tau is plotted against the di-tau mass approximated by the MMC algorithm, normalized to unit area. The events for the VBF H$\to \tau^-\tau^+$ physics process with $m_H = 125\,$GeV at $\sqrt{s} = 8\,$TeV are simulated using the POWHEG + PYTHIA 8 Monte Carlo generator. Events are required to fulfil the selection cuts as described in Section 5.3, listed in Table B.8.


Figure A.17: The cosine of the angle α between the leading and sub-leading tau is plotted against the di-tau mass approximated by the MMC algorithm, normalized to unit area, where α is the three dimensional angle between the momentum vectors of the two tau leptons. The events for the VBF H$\to \tau^-\tau^+$ physics process with $m_H = 125\,$GeV at $\sqrt{s} = 8\,$TeV are simulated using the POWHEG + PYTHIA 8 Monte Carlo generator. Events are required to fulfil the selection cuts as described in Section 5.3, listed in Table B.8.
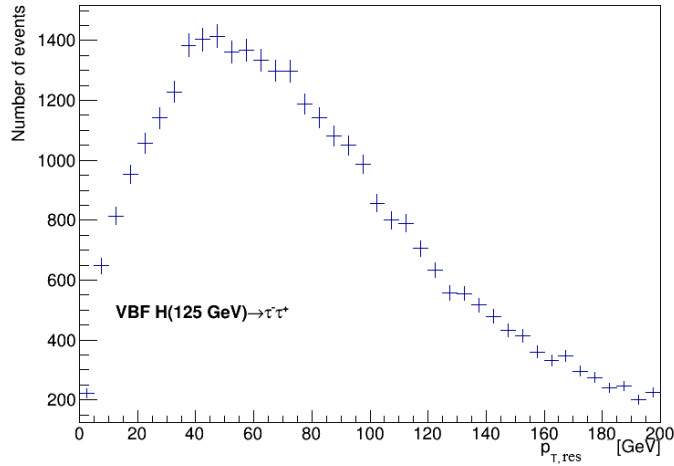
Figure A.18: The variable ΔR between the leading and sub-leading tau is plotted against the di-tau mass approximated by the MMC algorithm, normalized to unit area The events for the gg H$\to \tau^- \tau^+$ physics process with $m_H = 125\,\text{GeV}$ at $\sqrt{s} = 8\,\text{TeV}$ are simulated using the POWHEG + PYTHIA 8 Monte Carlo generator. Events are required to fulfil the selection cuts as described in Section 5.3, listed in Table B.8.
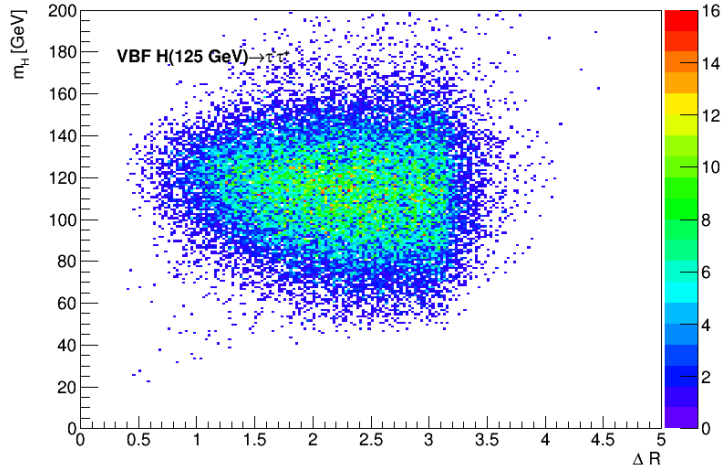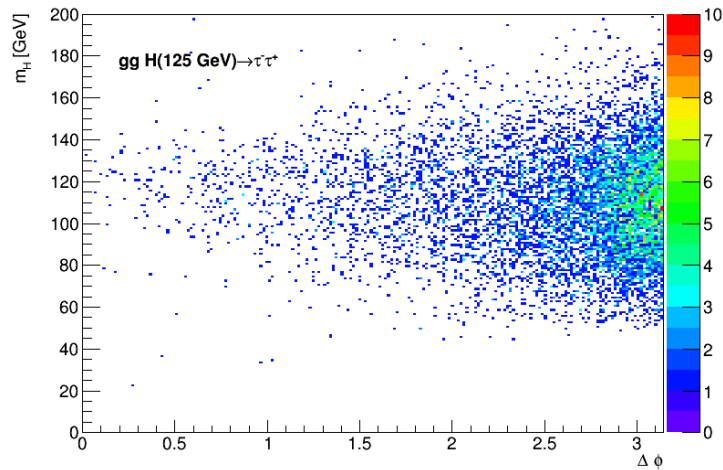

Figure A.19: The difference of the azimuthal angle $\Delta\phi$ between the leading and sub-leading tau is plotted against the di-tau mass approximated by the MMC algorithm, normalized to unit area The events for the gg H$\to \tau^- \tau^+$ physics process with $m_H = 125\,\text{GeV}$ at $\sqrt{s} = 8\,\text{TeV}$ are simulated using the POWHEG + PYTHIA 8 Monte Carlo generator. Events are required to fulfil the selection cuts as described in Section 5.3, listed in Table B.8.
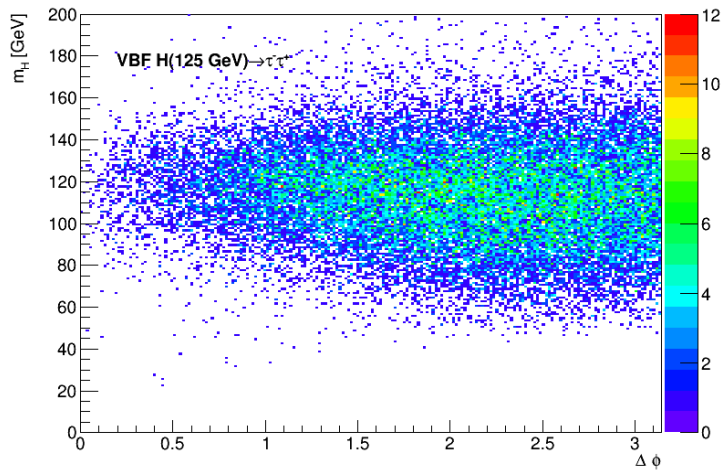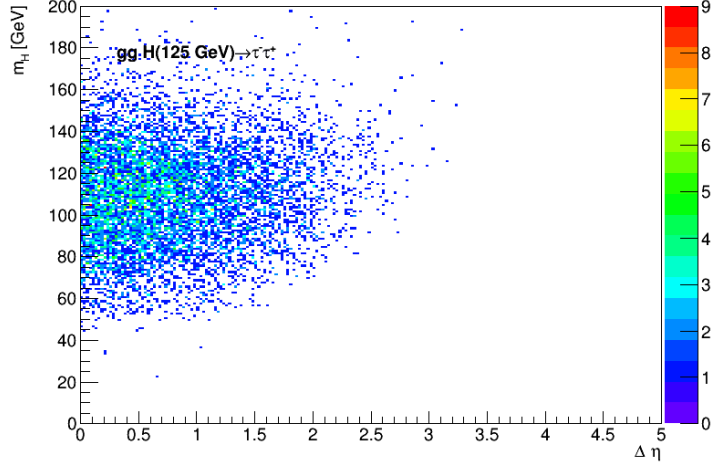
Figure A.20: The difference of the pseudo-rapidity $\Delta\eta$ between the leading and sub-leading tau is plotted against the di-tau mass approximated by the MMC algorithm, normalized to unit area The events for the gg H$\to \tau^-\tau^+$ physics process with $m_H = 125$ GeV at $\sqrt{s} = 8$ TeV are simulated using the POWHEG + PYTHIA 8 Monte Carlo generator. Events are required to fulfil the selection cuts as described in Section 5.3, listed in Table B.8.
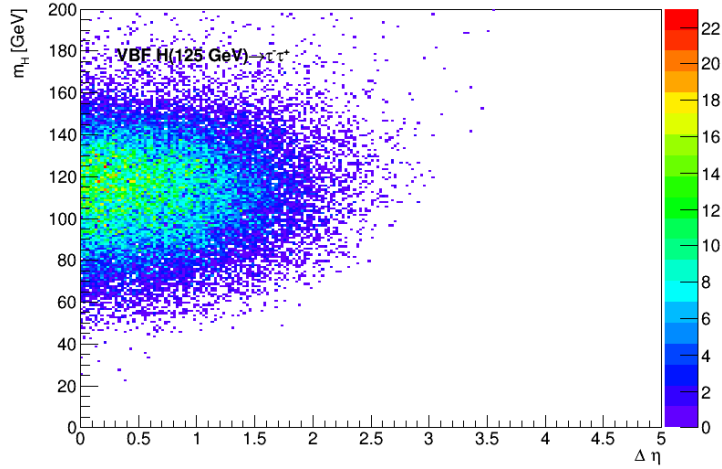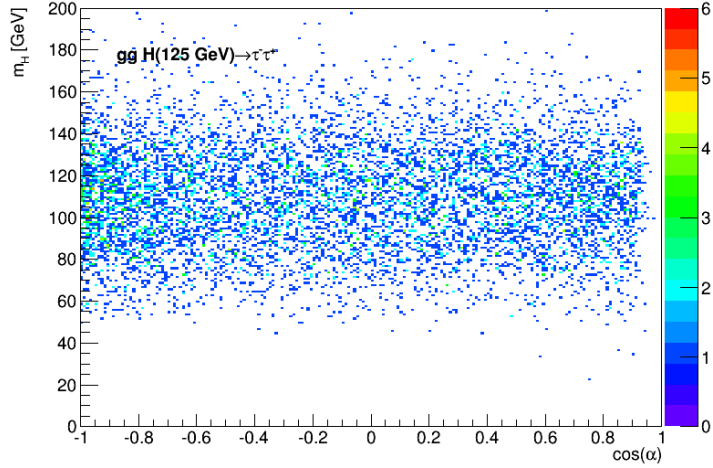

Figure A.21: The cosine of the angle α between the leading and sub-leading tau is plotted against the di-tau mass approximated by the MMC algorithm, normalized to unit area,, where α is the three dimensional angle between the momentum vectors of the two taus. The events for the gg H$\to \tau^-\tau^+$ physics process with $m_H = 125$ GeV at $\sqrt{s} = 8$ TeV are simulated using the POWHEG + PYTHIA 8 Monte Carlo generator. Events are required to fulfil the selection cuts as described in Section 5.3, listed in Table B.8.
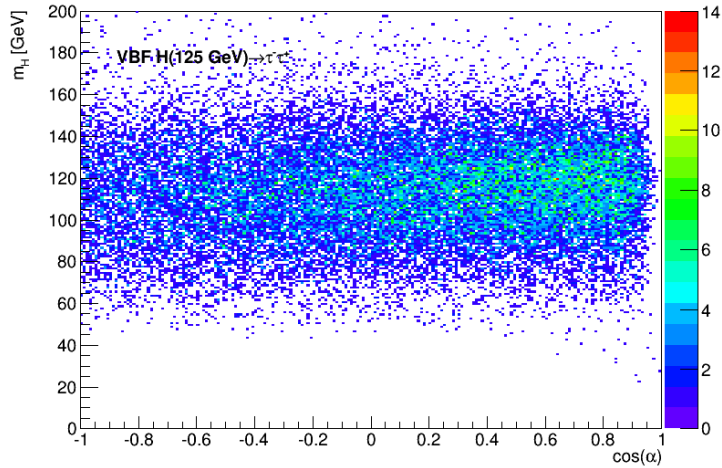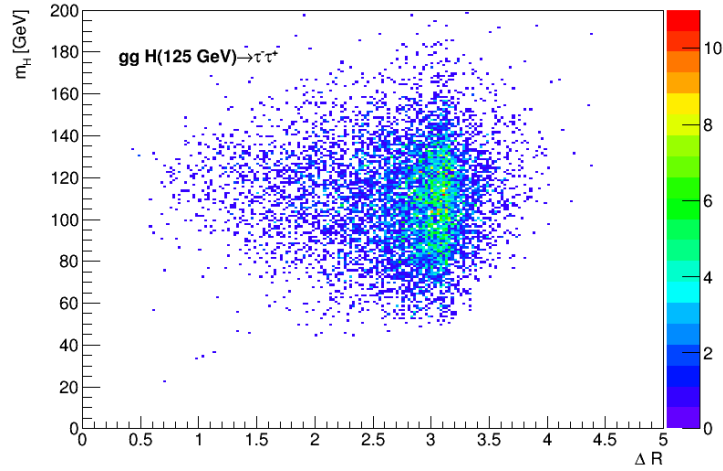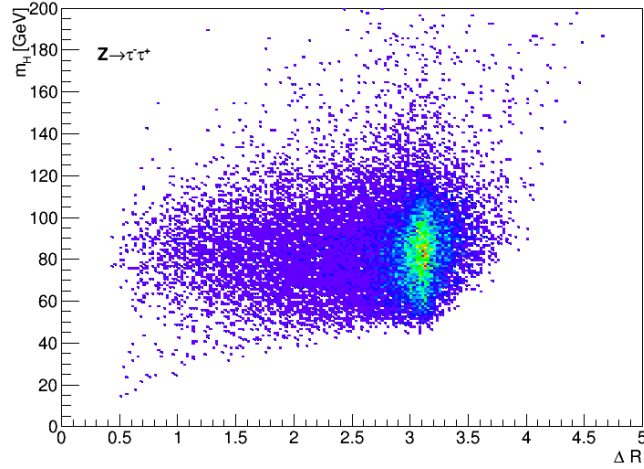
Figure A.22: The variable ΔR between the leading and sub-leading tau is plotted against the di-tau mass approximated by the MMC algorithm, normalized to unit area The events for the $Z \to \tau^- \tau^+$ physics process at $\sqrt{s} = 8\,\mathrm{TeV}$ are simulated using the ALPGEN +JIMMY Monte Carlo generator. Events are required to fulfil the selection cuts as described in Section 5.3, listed in Table B.8.

Figure A.23: The difference of the pseudorapidites $\Delta \eta$ between the leading and sub-leading tau is plotted against the di-tau mass approximated by the MMC algorithm, normalized to unit area The events for the $Z \to \tau^- \tau^+$ physics process at $\sqrt{s} = 8\,\mathrm{TeV}$ are simulated using the ALPGEN +JIMMY Monte Carlo generator. Events are required to fulfil the selection cuts as described in Section 5.3, listed in Table B.8.

B Additional Tables

B.1 Tables for Chapter 4

Sample name	Abbreviation
NP0 Z$\rightarrow \tau^+\tau^-$ with $\sigma = 711810$ pb	
mc12_8TeV.107670.AlpgenJimmy_AUET2CTEQ6L1_ZtautauNp0.merge. NTUP_TAU.e1571_s1499_s1504_r3658_r3549_p1344_*	
*tid01189567_00/NTUP_TAU.01189567._000001.root.1	file1_NP0
*tid01189567_00/NTUP_TAU.01189567._000003.root.1	file2_NP0
*tid01189567_00/NTUP_TAU.01189567._000005.root.1	file3_NP0
*tid01189567_00/NTUP_TAU.01189567._000014.root.1	file4_NP0
*tid01258221_00/NTUP_TAU.01258221._000062.root.1	file5_NP0
*tid01258221_00/NTUP_TAU.01258221._000076.root.1	file6_NP0
*tid01258221_00/NTUP_TAU.01258221._000080.root.1	file7_NP0
*tid01258221_00/NTUP_TAU.01258221._000093.root.1	file8_NP0
*tid01258221_00/NTUP_TAU.01258221._000095.root.1	file9_NP0
*tid01258221_00/NTUP_TAU.01258221._000107.root.1	file10_NP0
*tid01258221_00/NTUP_TAU.01258221._000113.root.1	file12_NP0
*tid01258222_00/NTUP_TAU.01258222._000156.root.1	file12_NP0
*tid01258222_00/NTUP_TAU.01258222._000187.root.1	file13_NP0
*tid01258223_00/NTUP_TAU.01258223._000223.root.1	file14_NP0
*tid01258223_00/NTUP_TAU.01258223._000230.root.1	file15_NP0
*tid01258223_00/NTUP_TAU.01258223._000241.root.1	file16_NP0
*tid01258223_00/NTUP_TAU.01258223._000244.root.1	file17_NP0
*tid01258223_00/NTUP_TAU.01258223._000249.root.1	file18_NP0
*tid01258223_00/NTUP_TAU.01258223._000261.root.1	file19_NP0
Total number of events: 474999	

Table B.1: Data samples with corresponding abbreviation sorted by physics process.

Sample name	Abbreviation
NP1 Z$\to \tau^+\tau^-$ with $\sigma = 155130\,\text{pb}$	
mc12_8TeV.107671.AlpgenJimmy__AUET2CTEQ6L1__ZtautauNp1.merge. NTUP__TAU.e1571__s1499__s1504__r3658__r3549__p1344__*	
*tid01258224__00/NTUP__TAU.01258224.__000009.root.1	file1__NP1
*tid01258224__00/NTUP__TAU.01258224.__000011.root.1	file2__NP1
*tid01258224__00/NTUP__TAU.01258224.__000014.root.1	file3__NP1
*tid01258224__00/NTUP__TAU.01258224.__000016.root.1	file4__NP1
*tid01258224__00/NTUP__TAU.01258224.__000018.root.1	file5__NP1
*tid01258224__00/NTUP__TAU.01258224.__000019.root.1	file6__NP1
*tid01258224__00/NTUP__TAU.01258224.__000022.root.1	file7__NP1
*tid01258224__00/NTUP__TAU.01258224.__000024.root.1	file8__NP1
*tid01258224__00/NTUP__TAU.01258224.__000027.root.1	file9__NP1
*tid01258224__00/NTUP__TAU.01258224.__000028.root.1	file10__NP1
*tid01258224__00/NTUP__TAU.01258224.__000029.root.1	file11__NP1
*tid01258224__00/NTUP__TAU.01258224.__000030.root.1	file12__NP1
*tid01258224__00/NTUP__TAU.01258224.__000034.root.1	file13__NP1
*tid01258224__00/NTUP__TAU.01258224.__000035.root.1	file14__NP1
*tid01258224__00/NTUP__TAU.01258224.__000038.root.1	file15__NP1
*tid01258224__00/NTUP__TAU.01258224.__000039.root.1	file16__NP1
*tid01258224__00/NTUP__TAU.01258224.__000043.root.1	file17__NP1
*tid01258224__00/NTUP__TAU.01258224.__000046.root.1	file18__NP1
*tid01258224__00/NTUP__TAU.01258224.__000047.root.1	file19__NP1
*tid01258224__00/NTUP__TAU.01258224.__000049.root.1	file20__NP1
*tid01258224__00/NTUP__TAU.01258224.__000052.root.1	file21__NP1
Total number of events: 524999	

Table B.2: Data samples with corresponding abbreviation sorted by physics process.

Sample name	Abbreviation
NP2 Z→ $\tau^+\tau^-$ with $\sigma = 48804\,\text{pb}$	
mc12_8TeV.107672.AlpgenJimmy_AUET2CTEQ6L1_ZtautauNp2.merge.* NTUP_TAU.e1571_s1499_s1504_r3658_r3549_p1344_*	
*tid01189569_00/NTUP_TAU.01189569._000001.root.1	file1_NP2
*tid01189569_00/NTUP_TAU.01189569._000002.root.1	file2_NP2
*tid01189569_00/NTUP_TAU.01189569._000003.root.1	file3_NP2
*tid01189569_00/NTUP_TAU.01189569._000004.root.1	file4_NP2
*tid01258225_00/NTUP_TAU.01258225._000005.root.1	file5_NP2
*tid01258225_00/NTUP_TAU.01258225._000006.root.1	file6_NP2
*tid01258225_00/NTUP_TAU.01258225._000008.root.1	file7_NP2
*tid01258225_00/NTUP_TAU.01258225._000010.root.1	file8_NP2
*tid01258225_00/NTUP_TAU.01258225._000013.root.1	file9_NP2
*tid01258225_00/NTUP_TAU.01258225._000017.root.1	file10_NP2
Total number of events: 229999 with $\sigma = 14160\,\text{pb}$	
NP3 Z→ $\tau^+\tau^-$	
mc12_8TeV.107673.AlpgenJimmy_AUET2CTEQ6L1_ZtautauNp3.merge. NTUP_TAU.e1571_s1499_s1504_r3658_r3549_p1344_*	
*tid01189570_00/NTUP_TAU.01189570._000001.root.1	file1_NP3
*tid01189570_00/NTUP_TAU.01189570._000002.root.2	file2_NP3
*tid01258226_00/NTUP_TAU.01258226._000003.root.1	file3_NP3
*tid01258226_00/NTUP_TAU.01258226._000004.root.1	file4_NP3
*tid01258226_00/NTUP_TAU.01258226._000005.root.1	file5_NP3
Total number of events: 1100000	
NP4 Z→ $\tau^+\tau^-$ with $\sigma = 3774.4\,\text{pb}$	
mc12_8TeV.107674.AlpgenJimmy_AUET2CTEQ6L1_ZtautauNp4.merge. NTUP_TAU.e1571_s1499_s1504_r3658_r3549_p1344_*	
*tid01189571_00/NTUP_TAU.01189571._000001.root.1	file1_NP4
*tid01258227_00/NTUP_TAU.01258227._000002.root.1	file2_NP4
Total number of events: 30000	
NP5 Z→ $\tau^+\tau^-$ with $\sigma = 1116.3\,\text{pb}$	
mc12_8TeV.107675.AlpgenJimmy_AUET2CTEQ6L1_ZtautauNp5.merge. NTUP_TAU.e1571_s1499_s1504_r3658_r3549_p1344_*	
tid01189572_00/NTUP_TAU.01189572._000001.root	file1_NP5
Total number of events: 1000	

Table B.3: Data samples with corresponding abbreviation sorted by physics process.

Sample name	Abbreviation
gg H(125 GeV)$\to \tau^+\tau^-$	
mc12_8TeV.161577.PowHegPythia8_AU2CT10_ggH125_tautauhh.merge. NTUP_TAU.e1217_s1469_s1470_r5470_r4540_p1344_*	
*tid01463624_00/NTUP_TAU.01463624._000001.root.1	file1_gg
*tid01463624_00/NTUP_TAU.01463624._000002.root.1	file2_gg
*tid01463624_00/NTUP_TAU.01463624._000003.root.1	file3_gg
*tid01463624_00/NTUP_TAU.01463624._000004.root.1	file4_gg
*tid01463624_00/NTUP_TAU.01463624._000005.root.1	file5_gg
*tid01463624_00/NTUP_TAU.01463624._000006.root.1	file6_gg
*tid01463624_00/NTUP_TAU.01463624._000007.root.1	file7_gg
*tid01463624_00/NTUP_TAU.01463624._000008.root.1	file8_gg
*tid01463624_00/NTUP_TAU.01463624._000009.root.1	file9_gg
*tid01463624_00/NTUP_TAU.01463624._000010.root.1	file10_gg
Total number of events: 100000	
VBF H(125 GeV)$\to \tau^+\tau^-$	
mc12_8TeV.161617.PowHegPythia8_AU2CT10_VBFH125_tautauhh.merge. NTUP_TAU.e1217_s1469_s1470_r3542_r3549_p1344_*	
*tid01108707_00/NTUP_TAU.01108707._000002.root.1	file1_VBF125
*tid01108707_00/NTUP_TAU.01108707._000003.root.2	file2_VBF125
*tid01108707_00/NTUP_TAU.01108707._000004.root.2	file3_VBF125
*tid01108710_00/NTUP_TAU.01108710._000041.root.1	file4_VBF125
*tid01108710_00/NTUP_TAU.01108710._000042.root.1	file5_VBF125
*tid01108710_00/NTUP_TAU.01108710._000043.root.1	file6_VBF125
*tid01108710_00/NTUP_TAU.01108710._000045.root.1	file7_VBF125
*tid01108710_00/NTUP_TAU.01108710._000047.root.1	file8_VBF125
*tid01108707_00/NTUP_TAU.01108707._000001.root.2	file9_VBF125
*tid01108709_00/NTUP_TAU.01108709._000025.root.1	file10_VBF125
*tid01108709_00/NTUP_TAU.01108709._000030.root.1	file11_VBF125
*tid01108711_00/NTUP_TAU.01108711._000056.root.1	file12_VBF125
Total number of events: 299997	

Table B.4: Data samples with corresponding abbreviation sorted by physics process.

Sample name	Abbreviation
VBF H$(120\,\mathrm{GeV})\to \tau^+\tau^-$	
mc12_8TeV.161616.PowHegPythia8_AU2CT10_VBFH120_tautauhh.merge. NTUP_TAU.e1217_s1469_s1470_r3753_r3549_p1344_*	
*tid01414579_00/NTUP_TAU.01414579._000030.root.1	file1_VBF120
*tid01108706_00/NTUP_TAU.01108706._000005.root.1	file2_VBF120
*tid01108705_00/NTUP_TAU.01108705._000004.root.1	file3_VBF120
Total number of events: 75000	
VBF H$(135\,\mathrm{GeV})\to \tau^+\tau^-$	
mc12_8TeV.161619.PowHegPythia8_AU2CT10_VBFH135_tautauhh.merge. NTUP_TAU.e1217_s1469_s1470_r3542_r3549_p1344_*	
*tid01108715_00/NTUP_TAU.01108715._000005.root.1	file1_VBF135
*tid01108715_00/NTUP_TAU.01108715._000006.root.1	file2_VBF135
*tid01108715_00/NTUP_TAU.01108715._000010.root.1	file3_VBF135
Total number of events: 75000	
VBF H$(145\,\mathrm{GeV})\to \tau^+\tau^-$	
mc12_8TeV.161621.PowHegPythia8_AU2CT10_VBFH145_tautauhh.merge. NTUP_TAU.e1217_s1469_s1470_r3542_r3549_p1344_*	
*tid01108719_00/NTUP_TAU.01108719._000007.root.1	file1_VBF145
*tid01108719_00/NTUP_TAU.01108719._000010.root.1	file2_VBF145
*tid01435729_00/NTUP_TAU.01435729._000039.root.1	file3_VBF145
Total number of events: 75000	

Table B.5: Data samples with corresponding abbreviation sorted by physics process.

B.2 Tables for Chapter 5

Cut name	Passing condition
$C_{\tau,\text{reco}}$	$\eta_\tau < 2.5$, $p_{T,\tau} > 20\,\text{GeV}$
$C^1_{\tau,\text{ID}}$	author$= 1 \vee 3$, $n_{\text{tracks}} = 1 \vee 3$, no muon veto Jet/Sig BDT loose discriminant, Electron BDT loose discriminant
$C^2_{\tau,\text{ID}}$	$n_\tau > 1$ with $C_{\tau,\text{reco}}$ and $C^1_{\tau,\text{ID}}$ applied, $\tau_1 \vee \tau_2$ fulfil Jet/Sig BDT loose discriminant
$C_{\tau\tau}$	$n_\tau > 1$
$C_{\text{opp. sign}}$	The two leading taus have opposite charges.
C_{true}	$\Delta R < 0.2$ between truth tau and tau candidate.
C_{overlap}	$\Delta R < 0.2$ between jet and tau candidate.
$C^1_{\text{jet,reco}}$	$\eta_{\text{jet}} < 4.7$, $p_{T,\text{jet}} > 20\,\text{GeV}$
$C^2_{\text{jet,reco}}$	$\eta_{\text{jet}} < 4.7$, $p_{T,\text{jet}} > 25\,\text{GeV}$
C_{1jet}	$n_{\text{jets}} > 0$
C_{2jets}	$n_{\text{jets}} > 1$
C_{MMC}	The MMC algortihm is required to be applied successfully.
$C_{\slashed{E}_T\text{ int}}$	The missing transverse energy $\slashed{E}_T$ must lie between both taus.
$C_{\slashed{E}_T\text{ not int}}$	$C_{\slashed{E}_T\text{ in }\varphi}$ is not fulfilled.
$C_{\text{MMC},x_1 x_2}$	$0 < x_1, x_2 < 1$ of the MMC algorithm, which is equivalent to $C_{\slashed{E}_T\text{ int}}$.
$C_{\slashed{E}_T,\Delta\varphi}$	$\slashed{E}_T > 20\,\text{GeV}$, $\Delta\varphi_{\tau\tau} < \epsilon$
$C_{\text{Coll},x_1 x_2}$	$0 < x_1, x_2 < 1$ of the collinear approximation
C_{default}	The cuts $C_{\tau,\text{reco}}$, $C^1_{\tau,\text{ID}}$, $C^2_{\tau,\text{ID}}$, $C_{\tau\tau}$, $C_{\text{opp. sign}}$, $C^1_{\text{jet,reco}}$ must be fulfilled, overlap has been removed.
C_τ	The cuts $C_{\tau,\text{reco}}$, $C^1_{\tau,\text{ID}}$, $C^2_{\tau,\text{ID}}$, $C_{\tau\tau}$, $C_{\text{opp. sign}}$ must be fulfilled.
C_{all}	C_{default}, C_{MMC} and ($C_{\slashed{E}_T\text{ int}}$ or $C_{\text{Coll},x_1 x_2}$) (depending on what reconstruction method is used) must be fulfilled.

Table B.6: Selection criteria named and listed.

Parameter	Value
SetCalibrationSet	MMCCalibrationSet::MMC2012 (tag 00-15)
SetUseVerbose	0
SetNsigmaMETscan	4.0
SetUseTailCleanup	0
SetAlgorithmVersion	1
SetNiterFit2	40

Table B.7: Input parameters for the MMC algorithm.

Histogram	Cuts applied
Basic tau kinemtic control plots from 5.1 to A.6	C_τ
A.7, A.9 and A.11	$C_{default}$
A.8, A.10 and A.12	$C_{default}$, C_{MMC}
All plots from A.13 to A.23	$C_{default}$, C_{MMC}
6.7 and 6.8	C_{all}
6.6	C_{all}
6.5, 6.3, 6.4	C_{all}
A.13	C_{all}
6.1, 6.2	C_{all}

Table B.8: Histograms listed with the individual cuts applied.

B.3 Tables for Chapter 6

Parameter	Value	Error
MMC algorithm		
Constant a	0.0873	0.0007
Mean μ [GeV]	113.8	0.2
Sigma σ' [GeV]	22.8	0.3
Collinear Approximation		
Constant a	0.0817	0.0008
Mean μ [GeV]	136.5	0.3
Sigma σ' [GeV]	22.5	0.3

Table B.9: Fit parameters of the Gaussian fit applied to the core distributions for the VBF sample.

Parameter	Value	Error
MMC algorithm		
Constant a	0.082	0.002
Mean μ [GeV]	108.9	0.4
Sigma σ' [GeV]	24.6	0.5
Collinear Approximation		
Constant a	0.065	0.002
Mean μ [GeV]	140.2	0.7
Sigma σ' [GeV]	30	1

Table B.10: Fit parameters of the Gaussian fit applied to the core distributions for the gg sample.

	Total events	Events after C$_{\mathbf{default}}$	MMC eff.	Coll. appr. eff.
Data sample for the Z$\rightarrow \tau^+\tau^-$ physics process				
NP0	474999	14287	43.17 %	43.25 %
NP1	524999	18572	48.05 %	48.69 %
NP2	229999	9113	48.29 %	49.34 %
NP3	110000	4558	47.59 %	49.12 %
NP4	30000	1292	46.21 %	47.52 %
NP5	10000	440	46.14 %	48.41 %
Data sample for the gg H$\rightarrow \tau^+\tau^-$ physics process				
$m_H =$ GeV	100000	17125	48.8 %	49.09 %
Data sample for the VBF H$\rightarrow \tau^+\tau^-$ physics process				
$m_H = 120$ GeV	75000	13829	58.09 %	58.82 %
$m_H = 125$ GeV	299997	57773	58.85 %	59.49%
$m_H = 135$ GeV	75000	15746	60.96 %	60.29 %
$m_H = 145$ GeV	75000	16502	60.56 %	59.87 %

Table B.11: Efficiencies of the two different mass reconstruction methods depending on the physics process and the data sample used.

Bibliography

[1] D. Griffiths, *Introduction to Elementary Particles*, Physics textbook, Wiley (2008)

[2] P. W. Higgs, *Broken Symmetries and the Masses of Gauge Bosons*, Phys. Rev. Lett. **13**, 508 (1964)

[3] F. Englert, R. Brout, *Broken Symmetry and the Mass of Gauge Vector Mesons*, Phys. Rev. Lett. **13**, 321 (1964)

[4] G. S. Guralnik, et al., *Global Conservation Laws and Massless Particles*, Phys. Rev. Lett. **13**, 585 (1964)

[5] M. Endres, et al., *The 'Higgs' Amplitude Mode at the Two-Dimensional Superfluid-Mott Insulator Transition*, Nature **487**, 454 (2012)

[6] M. Srednicki, *Quantum Field Theory*, Cambridge University Press (2007)

[7] ATLAS Collaboration, Aad, G. et al., *The ATLAS Experiment at the CERN Large Hadron Collider*, JINST **3**, S08003 (2008)

[8] O. S. Bruning, et al., *LHC Design Report. 1. The LHC Main Ring*, CERN-2004-003-V-1, CERN-2004-003 (2004)

[9] ATLAS Collaboration, Aad, G. et al., *Studies of the performance of the ATLAS detector using cosmic-ray muons*, Eur. Phys. J. **C71**, 1593 (2011)

[10] D. E. Groom, et al., *Muon stopping power and range tables 10 MeV-100 TeV*, Atomic Data and Nuclear Data Tables **78(2)**, 183 (2001)

[11] A. D. Martin, *Parton distributions of the proton*, Phys. Rev. D **50**, 6734 (1994)

[12] *Review of Particle Physics*

[13] S. Glashow, *Partial Symmetries of Weak Interactions*, Nucl. Phys. **22**, 579 (1961)

[14] A. Salam, *Weak and Electromagnetic Interactions*, Conf. Proc. **C680519**, 367 (1968)

Bibliography

[15] S. Weinberg, *A Model of Leptons*, Phys. Rev. Lett. **19**, 1264 (1967)

[16] F. Hasert, et al., *Search for elastic muon-neutrino electron scattering*, Phys. Lett. B **46(1)**, 121 (1973)

[17] F. Hasert, et al., *Observation of neutrino-like interactions without muon or electron in the gargamelle neutrino experiment*, Phys. Lett. **46(1)**, 138 (1973)

[18] G. Arnison, et al., *Experimental observation of isolated large transverse energy electrons with associated missing energy at $\sqrt{s} = 540\,GeV$*, Phys. Lett. B **122(1)**, 103 (1983)

[19] *Observation of single isolated electrons of high transverse momentum in events with missing transverse energy at the Cern pp collider*

[20] Atlas Collaboration, Aad, G. et al., *Observation of a new particle in the search for the Standard Model Higgs boson with the Atlas detector at the Lhc*, Phys. Lett. B **716(1)**, 1 (2012)

[21] Cms Collaboration, S. Chatrchyan et al., *Observation of a new boson at a mass of 125 GeV with the Cms experiment at the Lhc*, Phys. Lett. B **716(1)**, 30 (2012)

[22] Cms Collaboration, S. Chatrchyan et al., *Evidence for the direct decay of the 125 GeV Higgs boson to fermions*, Nature Phys. **10** (2014)

[23] Atlas Collaboration, *Evidence for Higgs Boson Decays to the $\tau^+\tau^-$ Final State with the Atlas Detector*, Technical Report Atlas-CONF-2013-108, Cern, Geneva (2013)

[24] Lhc Higgs Cross Section Working Group, *Handbook of Lhc Higgs Cross Sections: 3. Higgs Properties* (2013)

[25] M. L. Perl, et al., *Evidence for Anomalous Lepton Production in e^+-e^- Annihilation*, Phys. Rev. Lett. **35**, 1489 (1975)

[26] A. Elagin, others., *A New Mass Reconstruction Technique for Resonances Decaying to di-tau*, Nucl. Instrum. Meth. **A654**, 481 (2011)

[27] Geant 4, *Geant 4: A Simulation toolkit*, Nucl. Instrum. Meth. **A506**, 250 (2003)

[28] J. Allison, et al., *Geant4 developments and applications*, IEEE Trans. Nucl. Sci. **53**, 270 (2006)

[29] Z. Bern, et al., *Ntuples for NLO Events at Hadron Colliders*, Comput. Phys. Commun. **185**, 1443 (2014)

[30] P. Nason, C. Oleari, *NLO Higgs boson production via vector-boson fusion matched with shower in* Powheg, JHEP **1002**, 037 (2010)

[31] S. Alioli, et al., *NLO Higgs boson production via gluon fusion matched with shower in*Powheg, JHEP **0904**, 002 (2009)

[32] T. Sjostrand, et al., *A Brief Introduction to* Pythia *8.1*, Comput. Phys. Commun. **178**, 852 (2008)

[33] M. Moretti, *A New approach to multijet calculations in hadron collisions*, Nucl. Phys. Proc. Suppl. **89**, 190 (2000)

[34] M. L. Mangano, et al., *Multijet matrix elements and shower evolution in hadronic collisions: $W b\bar{b} + n$ jets as a case study*, Nucl. Phys. **B632**, 343 (2002)

[35] M. L. Mangano, et al., Alpgen*, a generator for hard multiparton processes in hadronic collisions*, JHEP **0307**, 001 (2003)

[36] G. Corcella, I. Knowles, G. Marchesini, S. Moretti, K. Odagiri, et al., Herwig *6.5 release note* (2002)

[37] B. P. Roe, et al., *Boosted decision trees, an alternative to artificial neural networks*, Nucl. Instrum. Meth. **A543**, 577 (2005)

[38] M. Thomson, *Modern Particle Physics*, Modern Particle Physics, Cambridge University Press (2013)

Acknowledgments

I would like to thank Prof. Dr. Arnulf Quadt for enabling me to work on a bachelors thesis in such an interesting field of physics. I would also like to thank Prof. Dr. Ariane Frey for correcting this thesis as the second referee. For the much needed help in the beginning, proofreading in the end and patiently taking care of the never ending stream of questions and problems I would like to thank Dr. Zinonas Ziononos. Dr. Ulla Blumenschein also took care of many problems and offered time and explanations on my way to this thesis, I would like to thank her for this and for proofreading this thesis. Another thank you goes to the remaining members of the Higgs group in Göttingen, Eric Drechsler and Simon Schulte, for the constructive criticism in the meetings and to Tom Bednall for also proofreading this work.

I would like to thank Ann-Kristin Lohmann for proofreading and for the motivation and encouragement she offered me. Furthermore, I would like to thank all the other Bachelor students, namely Timo Dreyer, Jens Oltmanns, Fabian Sohns and Felix Wiebe, for listening to all of my complaints and for keeping up a great working morale throughout the course of this semester.

Lastly, I would like to thank my family for encouraging me in hard times and for occasionally taking my mind off of the university, allowing me to collect my thoughts and regain my spirits.

Erklärung   nach §13(8) der Prüfungsordnung für den Bachelor-Studiengang Physik und den Master-Studiengang Physik an der Universität Göttingen:

Hiermit erkläre ich, dass ich diese Abschlussarbeit selbständig verfasst habe, keine anderen als die angegebenen Quellen und Hilfsmittel benutzt habe und alle Stellen, die wörtlich oder sinngemäß aus veröffentlichten Schriften entnommen wurden, als solche kenntlich gemacht habe.

Darüberhinaus erkläre ich, dass diese Abschlussarbeit nicht, auch nicht auszugsweise, im Rahmen einer nichtbestandenen Prüfung an dieser oder einer anderen Hochschule eingereicht wurde.

<div align="center">Göttingen, den 18. Juli 2014</div>

<div align="center">(Art Gabriel)</div>